ICWE Investigations of Thermomechanical Responses in FSP and PVP Failure

A Dissertation Presented for the

Doctor of Philosophy

Degree

The University of Tennessee, Knoxville

Christian Andrew Kocak

December 2025

ACKNOWLEDGEMENTS

This research would not have been possible without the use of resources at the High Flux Isotope Reactor (HFIR), a DOE Office of Science User Facility operated by the Oak Ridge National Laboratory (ORNL). Funding for this project was provided by Shell Global Solutions and DEVCOM Ground Vehicle Systems Center, and made possible through the US National Science Foundation, Industry University Cooperative Research Center (I/UCRC) program, to the University of Tennessee under the Manufacturing and Materials Joining Innovation Center (Ma2JIC). Kocak also acknowledges the UT-ORII Energy Efficiency & Renewable Energy (EERE) Fellowship Program from the Department of Energy, the Tickle Graduate Fellowship program from Tickle College of Engineering, and the Graduate Advancement, Training and Education (GATE) Fellowship Program from the University of Tennessee-Oak Ridge Innovation Institute for funding support as well. Support and guidance were provided by major advisor Prof. Zhili Feng, co-advisor Prof. Yanfei Gao, industry mentors Dr. Jorge Penso and Mr. Martin McDonnell, instrument scientists Dr. Jeffery Bunn and Dr. Andrew Payzant, ORNL staff Dr. Yiyu Wang, Mr. Alan A. Frederick, and Mr. Doug J. Kyle, and fellow students Dr. Xue Wang, Dr. Hyojin Park, Dr. Di Xie, Dr. Joshua Kincaid, Mr. Elijah Charles, Ms. Lia Amilia, Dr. Yi Yang, and Dr. Dong Han, as well as advisors to some of these students Prof. Hahn Choo and Prof. Tony Schmitz, who provided experimental data. Much gratitude is extended to the thesis committee members, Prof. Zhili Feng, Prof. Yanfei Gao, Prof. Bradley Jared, and Dr. Jeffrey Bunn. Wife, Catherine, and dog, Tippit, as well as other family and friends, are also recognized for providing much needed emotional support.

ABSTRACT

Since the Second Industrial Revolution, welding has been an important technique in the engineering toolbox. Novel methods spawn and branch out, offering options each with their own strengths and weaknesses. Constant advancement of technology demands improvements of the methods used in fabrication. Integrated Computational Welding Engineering (ICWE) is a relatively new approach for accelerating understanding of the processing-microstructure-properties relationship for linking welding parameters to weldment performance. This work explores three examples of how ICWE can be used to solve real-world industry issues. Friction Stir Welding (FSW) and Additive Friction Stir Deposition (AFSD) are widely accepted joining techniques, yet mechanisms related to surface conditions, high-stress/temperature deformation, and bonding are not fully understood. In addition, premature failures in pressure vessels and piping systems (PVP) have been attributed to stress relaxation cracking. Trust in accelerated testing, incorporated into initial guidelines, led to premature failure. Understanding how weld behavior changes over different time, temperature, and stress ranges is required to make more accurate predictions. Residual stress fields remain a difficult feature to model and measure with confidence. The use of a plane stress assumption, typically reserved for analyzing stress of thin sheets, is applied to larger bulk structures when measuring residual stress using neutron diffraction.

TABLE OF CONTENTS

LIST OF TABLES

LIST OF FIGURES

Chapter 1

Introduction

1.1 Motivation

Regarding fabrication, a weld can reduce costs and grant freedom in the design of a structure. However, a joint will typically be the weakest point of a structure, and therefore generally be the location of failure. When metals are processed through forming (rolling, extrusion, etc.) a relatively homogenous microstructure can be engineered. Welding materials will inherently create heterogeneity of the microstructure, and therefore properties. A weld can be characterized by joint efficiency, or a ratio of the strength of the weld compared to the base material. The mismatch in material behavior will always result in a reduction of strength, but consequences can be minimized through an understanding of metallurgy, thermodynamics, and mechanics of materials. Acknowledgement of the limits of joining is key to designing structures that resist failure due to localized material degradation. This work demonstrates that by expanding the understanding of mechanisms that govern weld performance, process development can be accelerated while catastrophic failures can be avoided.

The most common branch of welding is fusion welding where adjoining metal surfaces are melted together. Melting can be done by directing energy at the workpieces or from the energy present in molten filler metal. The liquid metal wets to newly created solid surfaces free of an oxide layer. Using the solid surface as a collection of nucleation sites, the work pieces are made whole as the liquid cools and solidifies. A multitude of events occur during and following solidification. The steep thermal gradients create long textured grains, while residual stress fields can extend deep into the base metal. Elevated temperatures surrounding the weld can cause intermetallic compounds to reprecipitate, solid phases to transform, and grains to recrystallize. Welds are prone to forming defects such as porosity, lack of fusion, inclusions, and cracks. The degree of these events is dependent on the weld parameters and the composition of the metals. Ultimately, joint efficiency is dependent on compounding factors.

Prior to industrial welding, metal workers joined work pieces though forge welding, where solid metal was joined under sufficient heat and pressure. Recent decades have shown an increased interest in developing modern solid-state welding processes, due in part to temperatures remaining below the melting point. Solidification defects are absent, and the effects of high heat input are mitigated. However, industrial fusion techniques have existed for over a century and have been studied throughout this time frame. While newer solid-state methods offer potential benefits, the underlying mechanisms are yet to be fully investigated.

The transportation industry relies on high specific strength alloys to increase energy efficiency and reduce costs. Light-weight metallic elements typically have significantly lower yield strengths and rely on alloying and heat treatments to improve mechanical properties. The solidification and high heat from fusion processes reduce of an engineered microstructure and cause hot cracking. Mitigating loss of microstructural features such as fine-dispersed intermetallic compounds (IMC) or stable equiaxed multiphases can be achieved through by reducing heat input associated with solid-state processes. Additionally, dissimilar materials, which have poor weldability using fusion processes due to harmful large intergranular IMC formation, can potentially become weldable using solid-states processes that significantly reduce mixing across the joining interface.

However, these methods typically require large, automated welding units or setups that are not feasible for large-scale fabrication. The energy industry naturally opts for building larger power plants due to economic incentives and to shift efficiency limits set by thermodynamics. This means that large-scales systems are built on site and rely on professional welders using manual fusion techniques. The disadvantageous effects of fusion welding become a critical concern, especially considering plants are expected to operate on decade timescales at potentially elevated temperatures and/or high pressures.

1.2 Background

1.2.1 Integrated Computational Welding Engineering

The field of material science and engineering (MSE) is a broad subject with many branches. The MSE tetrahedron is a metaphoric model uniting each branch under a single philosophy. The corners of the tetrahedron are processing, structure, properties, and performance. At the center of the tetrahedron is characterization, or the methods used to describe each corner from observable information. The tetrahedron symbolizes how each corner is interconnected to all other corners. To truly build a framework for understanding relationships that form the tetrahedron, modeling techniques are used in tandem with data collected from characterization methods. Integrated Computational Welding Engineering (ICWE) is a field of applied science that aims to use incorporate both numerical and analytical methods across multiple length and time scales to build links in the MSE tetrahedron as it applies to welding. Welding parameters are a set of variables that often influence heat input, a central feature in welding processes. Challenges arise from variables often being coupled in a complex process parameter hyperspace through non-linear relationships. ICWE helps to construct frameworks that optimize welding processes by untangling the complexity of these relationships.

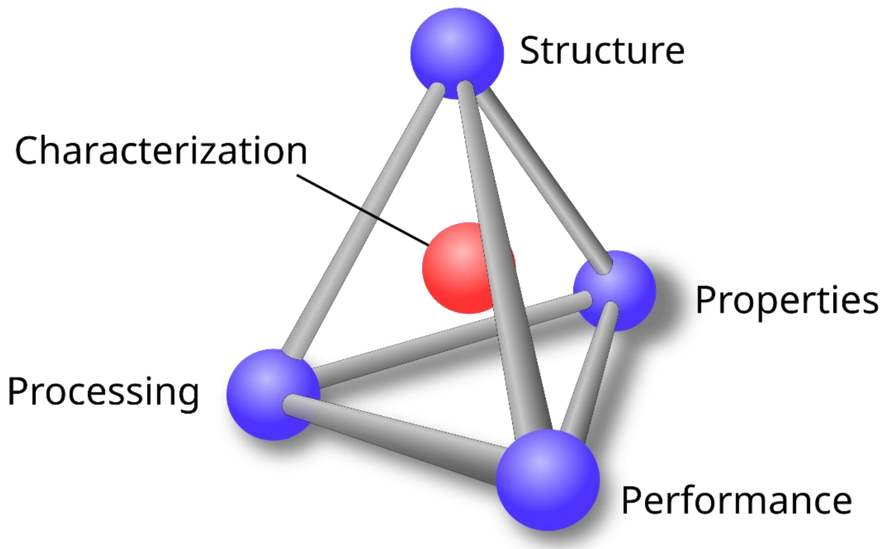

Figure 0.1 The Material Science and Engineering Tetrahedron

1.2.2 Friction Stir Processes

Friction Stir Welding (FSW) is a solid-state welding technique that was patented in 1991 by the Welding Institute [5]. A schematic of FSW is shown in Figure 1.2. A rotating, rigid tool with a flat shoulder is pressed into the workpieces. The applied load and torque on the tool cause frictional sliding and surface shearing at the tool-workpiece interface. The heat generated raises the temperature of the workpiece and plasticizes the material. Once enough heat is generated, the tool begins to travel, locally stirring the material of workpieces together. This process promotes metallic bonding of the workpieces by breaking up oxide layers and forcing voids created by the empty space in between asperities to collapse. The process was immediately implemented and improved through phenomenological advances, yet these sorts of approaches require extensive time and resources. Further advancement could be achieved by implementing an ICWE approach as computation and theory can be a quicker and low-cost alternative to experiments. Furthermore, thermomechanical responses are nearly impossible to comprehensively measure in an experimental setting and therefore require some sort of model to formulate field solutions. However, experimentation is still vital for model validation.

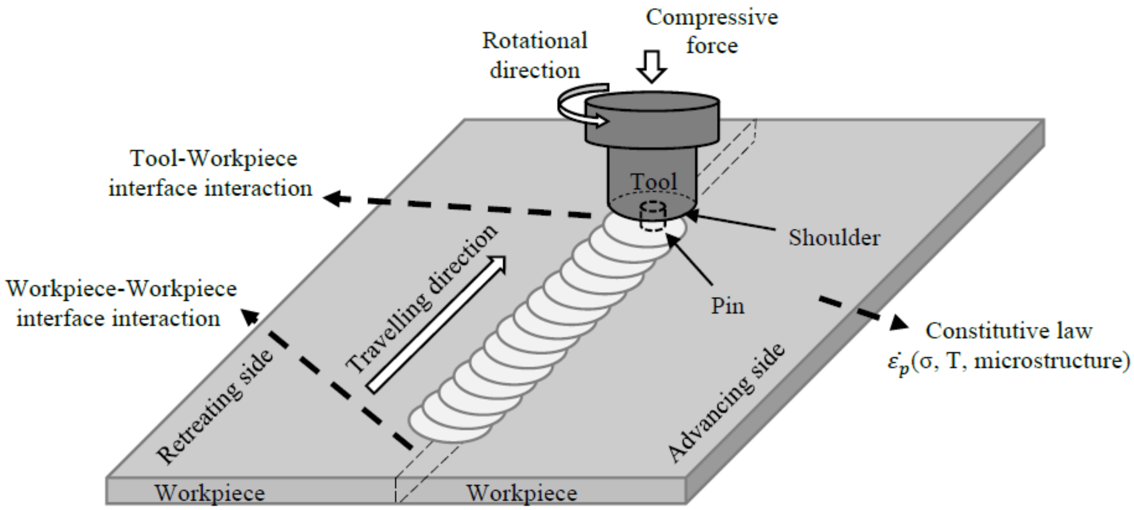

Figure 0.2. Schematic of FSW [19]

Interest in additively manufactured (AM) metallic components has steadily gained traction in recent years. Processes such as laser powder bed deposition (LPBD) and wire arc additive manufacturing (WAAM) are examples of popular metallic AM methods. Like welding, several technical difficulties arise from taking a fusion approach (e.g. porosity, high residual stress, high-quality powder required, spatter ejection, requiring a controlled atmosphere, and substrate warpage). Additive friction stir deposition (AFSD) is a process developed by the MELD Manufacturing Corporation in 2016 [7]. While built on previous friction-based additive processes, these predecessors have been hybrid methods requiring some significant subtractive process to arrive at the finished component. AFSD is the first additive friction-based process to achieve near-net-shaped components. A schematic of the concept can be seen in Figure 1.3.

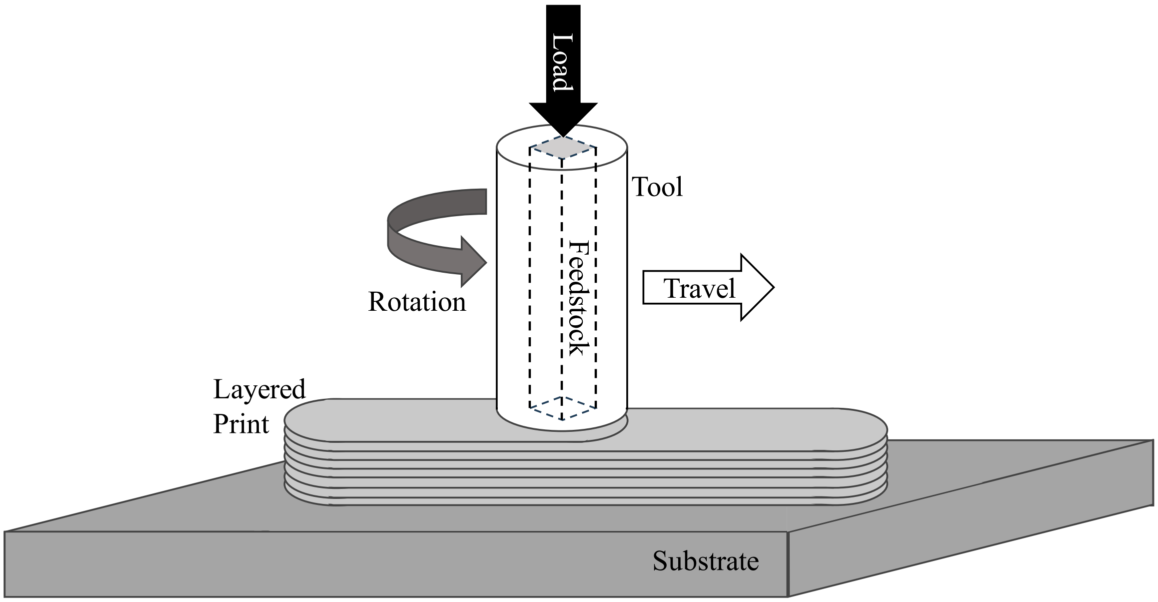

Figure 0.3 Schematic of AFSD

Based on the principles of friction stir cladding (FSC), ASFD involves the use of a hollow tool filled with feed material. The feed material used can be from a wider scope of alloys compared to fusion-based methods. Additionally, the process can accommodate material forms from low-quality powder to wrought bars. A torque load is applied to the tool along with a compressive axial load applied to the feed material using an actuator. As the tool rotates and the feedstock is pushed, the material is plasticized due to friction and plastic heating. The tool then traverses along a specified path depositing material along the way. The compressive load and the shear strain at the interface of the substrate or previous layer promote metallic bonding of the extruded feed material. The deposited material spreads out across an area roughly equivalent to the circular area of the shoulder, while the thickness of each layer is roughly equivalent to the gap between the shoulder and the work surface. Therefore, the in-plane resolution is limited to the tool size. However, this allows for relatively quick print speeds compared to other AM processes. This, combined with the fact that the process results in a fully dense part with a refined equiaxed grain structure, makes AFSD a good candidate for printing large-scale structural components. The material, while depositing, needs a surface to interact with, therefore only gradual slopes are possible.

1.2.3 Pressure Vessels & Piping

Mechanical engineering is a broad field like MSE. One of the roles of the American Society of Mechanical Engineers (ASME) is to provide codes and standards for engineering design. Pressure Vessels & Piping Division (PVP) technical division of ASME that focuses primarily on efficiency, reliability, and safety relating to pressure technology. The differences between pressure vessels and pipes are distinguished by function. Pressure vessels are designed to store fluids under pressure, while piping is a network of pipes and fittings designed to transport fluids under pressure. Together, with other components, they can be used to form large industrial systems. Welds are typically used to join, affix, and fabricate parts of these systems. As discussed, welds create heterogeneity within a structure that leads to a mismatch in properties. Therefore, understanding the effects of welding is crucial to the development of codes and standards that provided guidelines to design engineers and professional welders. Operating at elevated temperatures and non-ambient pressures can cause material at or near a weld degrade faster than the surrounding material. If unaddressed, damage can accumulate, and unexpected failure can occur.

The austenitic stainless steel 347H is a common alloy used for pressure vessels and piping in industrial settings (petrochemical, nuclear, etc.). This is due to its high weldability, creep resistance, and corrosion resistance. However, recurring failures of welded 347H pipes due to cracking have been observed in practice. Attributed to stress relief cracking (SRC), this can occur during the PWHT or while in-service at elevated temperatures [1]. The heat-affected zone (HAZ) is a region adjacent to the fusion zone (FZ) that does not melt but experiences significant microstructural evolution due to its proximity to the molten metal. The elevated temperatures promote grain growth and dissolution of precipitates. Upon reheating (PWHT or service conditions), relaxation occurs simultaneously with large carbide precipitation at grain boundaries. Precipitation of these larger carbides creates a thin region along the perimeter of the grains, deficient in alloying elements associated with fine dispersed precipitate strengthening. Therefore, this material has a lower yield strength compared to the bulk of the grain. These areas are known as precipitate free zones (PFZ). Stress can be resolved by plastically deforming these PFZ.

However, once a ductility limit is reached, cavities will start to form, followed by linkage/coalescence, and eventually lead to intergranular crack initiation.

Although this classical view of SRC is broadly understood, finer details remain to be fully explored. For example, whether cavity formation is governed by diffusion or creep, precipitate kinetics, etc. Existing empirical failure models are unreliable as they extrapolate from accelerated testing, whereas welds are expected to remain in service for decades. There is no guarantee that mechanisms will behave predictably at different time scales and temperatures ranges. This is supported by pervious work related to this project [11-17], which highlights the importance for mechanism-based lifetime predictions using modeling techniques, along with characterization efforts to refine the models.

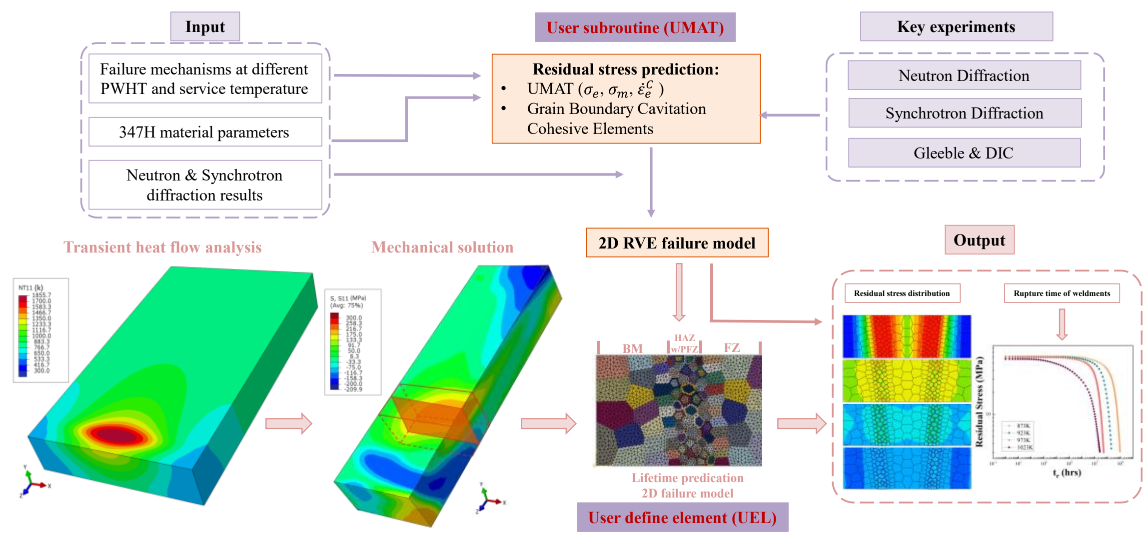

Figure 0.4 SRC ICWE framework for predicting lifetime of 347H weldments at various temperatures based on the presence of PFZs [17]

For example, in Figure 1.4. Yang et al. outline the modeling framework for residual stress formation and cavity failure, and how they can be linked to determine conditional SRC susceptibility and lifetime predictions in 347H. Additionally, Yang compiled data from accelerated failure testing plotted in Figure 1.5. The “C-curve” trends observed demonstrate that SRC susceptibility is governed by precipitate kinetics, while the relative differences in these curves emphasize the significant roles that both microstructure and thermomechanical state play.

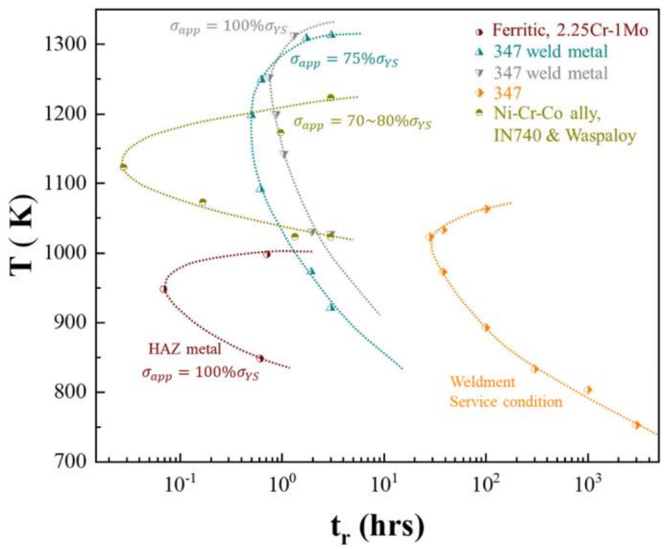

Figure 0.5 Stress-relaxation-cracking (SRC) susceptibility curves showing the temperature-lifetime relationship for various materials and their weldments, whereas some are subjected additional applied load and some are purely driven by welding-induced residual stress. Due to their shape, these curves are also called SRC C-curves. [17]

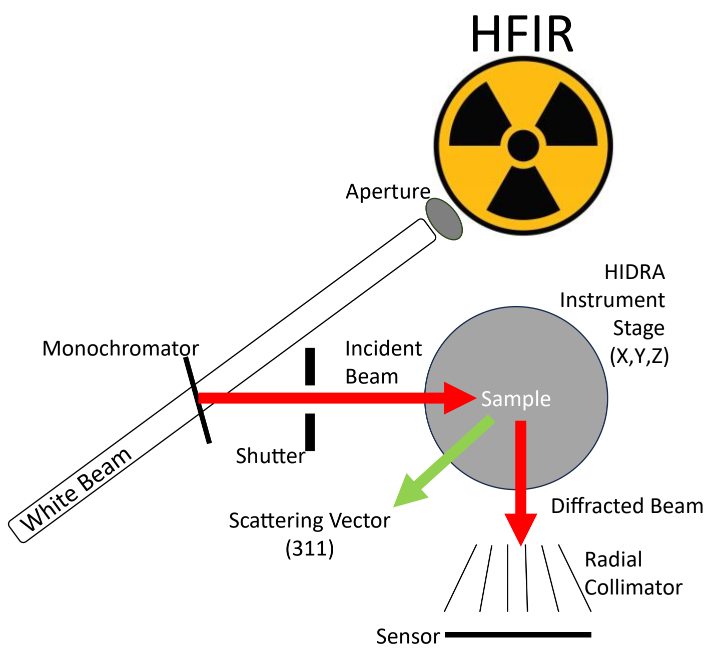

Figure 0.4 Schematic of HIDRA at the High Flux Isotope Reactor

Residual stress measurements are indirect, relying on measuring deformation, a consequence of residual stress, to relate back to stress. Destructive methods exist that measure how material reacts to being mechanically relieved, such as the sectioning technique, the contour method, hole-drilling, and the ring-core method. There are also non-destructive approaches like Barkausen noise and ultrasonic methods. However, Barkausen noise method requires a ferromagnetic medium and the ultrasonic method produces low resolution results. X-ray diffraction can produce high resolution results but can only collect surface-level data. Neutron diffraction is regarded as the one of most effective methods for mapping residual stress within a weld non-destructively, but neutron sources a scarce and difficult to access. While computational modeling can simulate residual stress, the penetrating capability of neutrons remains the best method to measure residual stress within a body, providing essential validation for modeling efforts. The schematic of the High Intensity Diffractometer for Residual stress Analysis (HIDRA) used in this research can be seen in Figure 1.6.

1.3 Scope of Research

Using ICWE, thermomechanical history can be estimated to build relationships from the MSE tetrahedron. We seek to apply this principle to FSW, AFSD, and SRC to solve real-world problems. In this work we predict:

- Using the established FSW ICWE framework, we can emulate the thermomechanical responses to predict bonding behavior in other cases and validate using existing experimental data. The extent of bonding can then be linked to performance (characterized by mechanical testing) to demonstrate the development of process windows.
- AFSD and FSW are fundamentally similar processes. With the established FSW ICWE framework, an understanding of the mechanical responses at friction surfaces exists. Using data collected from an AFSD controlled study, we can predict the heat generation rate and therefore the printing temperature when applying the Rosenthal Solution.
- A weld's processing parameters and heat treatment will affect the thermomechanical history and therefore determine both the microstructure

(cause of SRC) and residual stress (driving force of SRC). Residual stress characterization is difficult because statistical error in lattice spacing measurements can drastically alter the stress analysis and neutron sources are limited. We propose that a plane-stress geometric argument can be used to model the residual stress using only principal direction data to increase speed of experiments in some cases.

Chapter 2

Validation of Friction Stir Weld Models

The experimental work for the following chapter was performed by Dr. Hyojin Park under the advisement of Prof. Hahn Choo from the Department of Materials Science and Engineering. All experimental data and some of the visuals, especially those pertaining to the experimental work, were provided by Park.

2.1 Previous FSW Modeling Techniques Overview

While FSW is an effective method of joining, especially for historically low weldability alloy systems, mechanisms are not entirely understood. Wang proposes the following ICWE framework [18-20].

- An analytical solution to describe how rough surfaces can bond that is dependent on thermomechanical history.
- A theoretical explanation of the surface interactions and how they relate to heat generation, as well as a numerical method of predicting thermomechanical responses of the bulk based on those surface interactions.
- An ICWE framework capable of relating process parameters to weld performance based on the proposed methodology.

These FSW efforts are supported by comparing modeling results to literature data. However, using parametric-study data to validate models could be used to confirm assertions from the FSW ICWE framework. The proposed objectives of this research are to use data from an existing friction stir spot welding (FSSW) parametric study to compare to the modeling methods. FSSW is a subset of FSW that eliminates the travel step. While FSW can be used for either butt (like in Figure 1.1) or lap configurations, the typical application of FSSW is for lap welds only. Additionally, while previous modeling efforts focused on the aluminum alloy 6061, the experimental work was conducted on Ti-Al6-V4 (Ti64). This opportunity provides a unique challenge to test reworking numerical methods for a new process and material in addition to conducting model validation.

2.2 Literature Review

2.2.1 Analytical Modeling Techniques

To link processing to microstructure evolution, the effect of weld parameters on the thermomechanical history of the weld must be understood. During friction stir processes, heat is generated from both friction and plastic work. Heating is necessary to soften the metal enough to be mechanically worked. The plastic flow associated with stirring is necessary to bond workpieces together. The contact surface interactions will be either sticking (surface shearing), slipping (frictional heating), or, more realistically, a combination state. The ratio (c/a) of the surface area that is sticking versus slipping will determine the thermomechanical response.

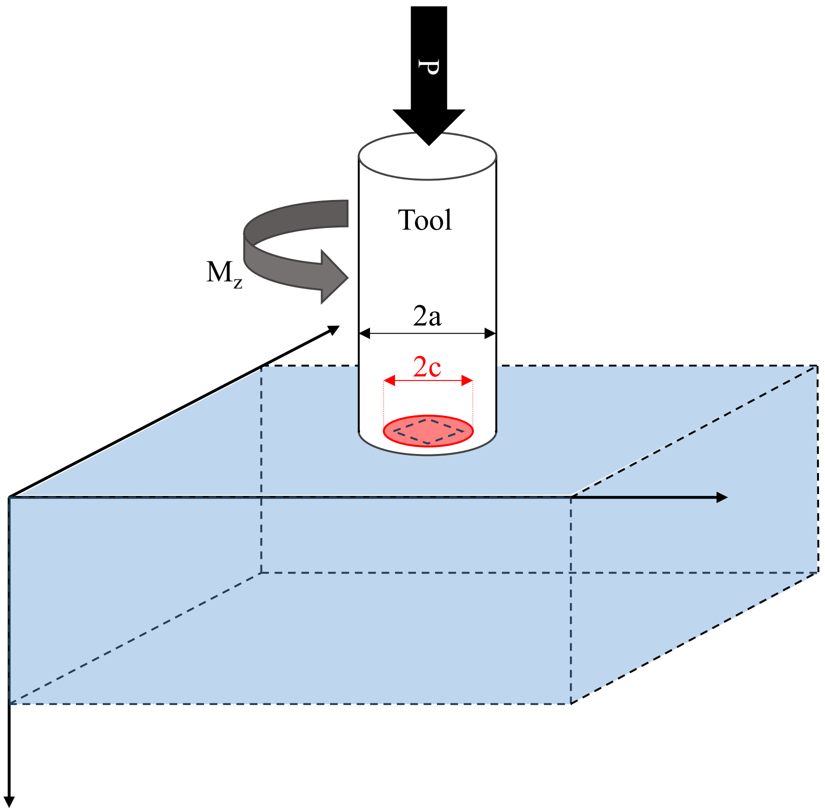

Figure 0.1 Schematic of stick-slip ratio in typical real case where 0 < c < a. The outer radius represents the radius of the tool. The inner radius is the radius of the stick region.

The total heat generation will be a summation of the frictional and plastic work converted to heat. By negating elastic deformation and assuming all plastic work is converted to heat, the total heat generation rate can be described by the sum of the area integrals [19].

$$Q_{total} = \int_{stick} \tau_{yield}\omega r \, dA + \int_{slip} \mu_f p\omega r \, dA \tag{1}$$

where p is the contact pressure, ω is the rotation speed of the tool, r is the size of the tool shoulder τ_{yield} is the shear yield strength, and μ_f is Coulomb's friction coefficient. Despite being composed of surface integral components, this equation accounts for plastic deformation in the bulk of the workpiece. Applying Gauss's theorem to the definition of heat generated due to plastic work can be used to redefine the equation as a surface integral because the divergence of the stress tensor is zero due to stress balance.

To know the heat generation rate, an analytical solution for the FSW torsional contact problem was derived. The contact pressure (P) is independent of the friction condition, therefore the interfacial shear stress due to friction can be described by Eq. 2.

$$\tau'_{\theta z} = \frac{\mu_f P}{2\pi a^2} \frac{1}{\sqrt{1-(r/a)^2}} \tag{2}$$

For infinite friction (sticking), the shear stress can be described by Eq. 3, where M^* is an unknown torque parameter

$$\tau_{\theta z}\big|_{\mu=\infty} = \frac{3M^*P}{4\pi a^3} \frac{r/a}{\sqrt{1-(r/a)^2}} \tag{3}$$

M^* can be solved for when the functions intersect at r = c.

$$\tau_{\theta z}\big|_{\mu=\infty} = \frac{\mu_f P}{2\pi a^2} \begin{cases} \dfrac{a}{c}\dfrac{r/a}{\sqrt{1-(r/a)^2}}, & r \le c: stick \\ \dfrac{1}{\sqrt{1-(r/a)^2}}, & c \le r \le a: slip \end{cases} \tag{4}$$

From this case, the subsequent torque can be found by integrating this function up to r = a. From the torque solution, Q_{total} can also be written in a dimensionless form.

$$\frac{Q_{total}}{\mu Pa\omega_0} = \frac{\omega}{\omega_0}\Pi_M(c/a) \tag{5}$$

Wang [19] demonstrated that $\Pi_M(c/a)$ showed a weak dependence on the surface conditions. From pure stick to pure slip, Π_M (c/a) fell within the range of 0.7-0.8. Therefore, a relation can be made between Q_{total}, M_z, and P.

$$Q_{total} \approx \omega M_z \approx \mu Pa\frac{3}{4} \tag{6}$$

Additionally, Eq.1 can be simplified to:

$$Q_{total} \approx \omega M_z \tag{7}$$

The traditional understanding of solid-state bonding for FSW assumes a diffusion mechanism similar to sintering. Wang [18] argues that predicted thermomechanical fields suggest that bonding locations remain mostly in a region dominated by Coble creep in deformation maps. This becomes an important consideration when developing a bonding model. Sham and Needleman have demonstrated how triaxial stress state can accelerate volumetric growth rate of voids during creep deformation. Wang offers a modified form of their equation (Eq. 8) that can be used to model the closure of voids due to the stress state, creep deformation, and temperature.

$$\frac{1}{f_b}\cdot\frac{df_b}{d_t} = -(1-f_b)\dot{\varepsilon}_{creep}^{eff} \times \begin{cases} \left[\alpha_n\left|\frac{\sigma_m}{\sigma_e}\right|+\beta_n\right]^n sgn\left(\frac{\sigma_m}{\sigma_e}\right), & if \left|\frac{\sigma_m}{\sigma_e}\right| > 1 \\ [\alpha_n+\beta_n]^n \frac{\sigma_m}{\sigma_e}, & if \left|\frac{\sigma_m}{\sigma_e}\right| \leq 1 \end{cases} \tag{8}$$

The f_b term is fraction of bonding with 0 being no bonding and 1 being full bonding, while $\dot{\varepsilon}$, σ_e, σ_m are effective creep strain rate, effective stress, and mean stress. Dimensional parameters α_n and β_n are $\alpha_n = 3n/2$ and $\beta_n = (n - 1)(n + 0.4319)n^{-2}$. The Needleman-Rice length scale was used to determine the governing deformation mechanism, seen below in Eq.9.

$$L_{NR} = \left[\frac{D_B\delta_B}{k_BT}\cdot\frac{\sigma_e}{\dot{\varepsilon}_{creep}^{eff}}\right]^{1/3} \tag{9}$$

D_B is the interfacial diffusion coefficient and δ_B is the interface boundary thickness. T is temperature and k_B is Boltzmann's constant. Additionally, the dominant deformation mechanism should determine how to model material behavior. Due to extreme stresses and temperatures, the hyperbolic sine law (Eq. 10) can be used as a constitutive model for FSP.

$$\dot{\varepsilon}_{creep} = A_n \left[\sinh\left(\frac{\sigma_e}{\sigma_{ref}}\right)\right]^n exp\left(-\frac{Q}{RT}\right) \tag{10}$$

A_n is a parameter, n is a stress exponent, Q is the creep activation energy, and R is the gas constant.

2.2.2 Numerical Modeling Techniques

Numerical methods have also been used to model thermomechanical features in FSW. Modeling stresses and strains in a body is typically done using computational solid mechanics (CSM). CSM is ideal for FSW as it can natively analyze interfacial interactions. As shown in equation 1, this is crucial for understanding heat generation. However, CSM cannot handle the severe deformation associated with FSW. An alternative method is to do an arbitrary Lagrangian-Eulerian (ALE) analysis. ALE iteratively remeshes during the simulation. However, the nearly convective nature of the material flow in FSW is still difficult to handle using ALE due to the instability of solution convergence and the computational cost of remeshing associated with the high degree of distortion. To manage the material flow, the metal can be treated like a non-Newtonian fluid using computational fluid dynamics CFD. The trouble in using CFD is it cannot inherently calculate the surface mechanics like CSM. Ad hoc boundary conditions can be prescribed to overcome this limitation. Another workaround would be a Coupled Eulerian-Lagrangian (CEL) approach, which uses both CSM and CFD meshes simultaneously. The volume fraction of metal is prescribed within an Eulerian domain initially while changes are tracked throughout the non-formable mesh during the simulation. The tool is modeled as a Lagrangian part that can interact with the workpiece to model the surface reactions. Although both methods can model the stick-slip behavior, the c/a values in the CFD models were sensitive to input parameters for the ad hoc interface models. Therefore, there are uncertainties, and determining reliable results is tedious.

2.3 Methodology: Friction Stir Spot Welding Parametric Study

2.3.1 Experiment Setup

Table 0.1 Welding parameters for FSSW parametric study

Sample ID	Rotation Speed (rpm)		Plunge speed (mm/s)	Plunge depth (mm)	Dwelling time (second)
A-1	2000	Step #01 (preheating)	0.212	0.637	5 s
		Step #02 (joining)	0.212	1.27	0 s
B-1	2250	Step #01 (preheating)	0.212	0.637	5 s
		Step #02 (joining)	0.212	1.27	0 s
C-1	2500	Step #01 (preheating)	0.212	0.637	5 s
		Step #02 (joining)	0.212	1.27	0 s
C-2	2500	Step #01 (preheating)	0.212	0.637	5 s
		Step #02 (joining)	0.127	1.27	0 s
C-3	2500	Step #01 (preheating)	0.212	0.637	5 s
		Step #02 (joining)	0.0423	1.27	0 s

The parametric FSSW experiment involves two steps: preheating and joining. The tool spins constantly throughout the process. To preheat, there is an initial plunge to a target depth of 0.636 mm at 0.212 mm/s. This parametric study investigates the effects of varying plunge rate (0.212, 0.127, and 0.0423 mm/s) at a constant tool rotation rate of 2500 RPM. Additionally, the rotation speed of the tool is varied (2000, 2250, and 2500 RPM) following the same joining plunge rate of 0.212 mm/s. The parameter overlap results in five weld parameter sets in total, as shown in Table 2.1.

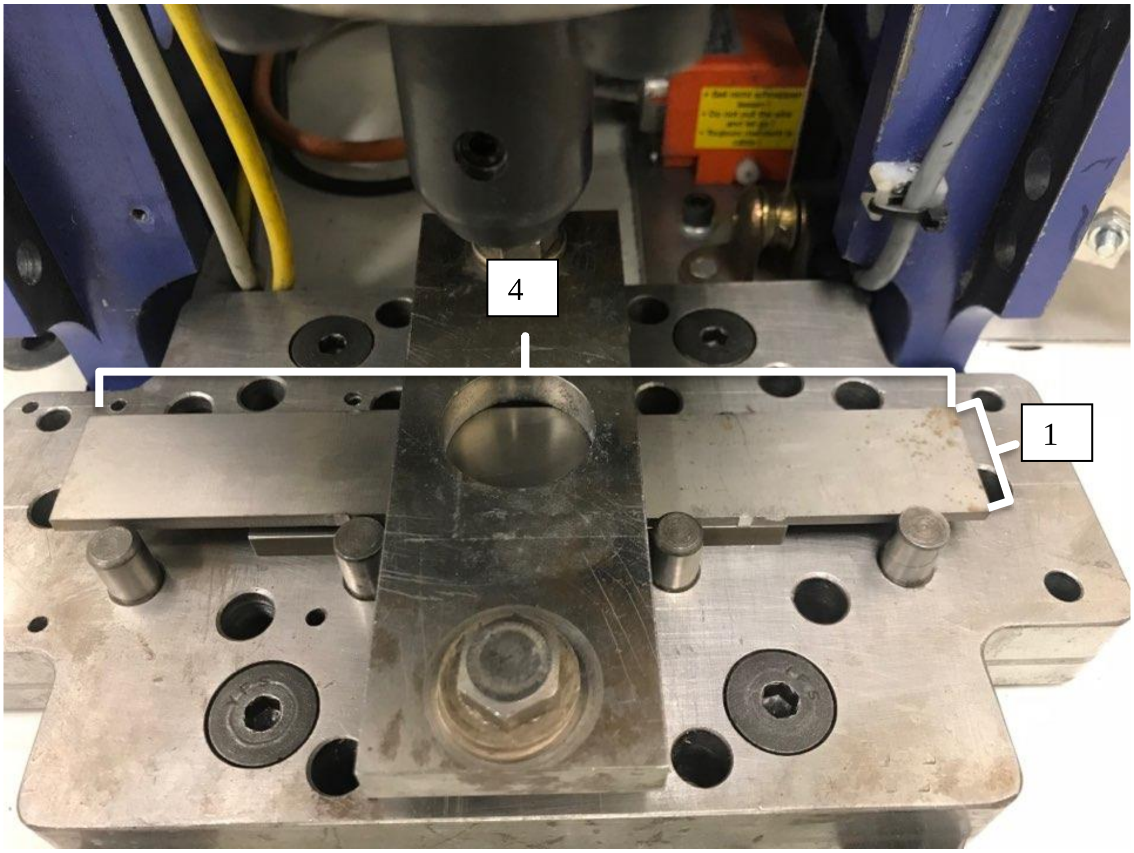

Figure 0.2 Two coupons overlapping by one inch (25.4mm) mounted on jig with backing plate

Two coupons of Ti64 (4” x 1” x 1/8”, 25.4 x 101.6 x 6.35 mm) were mounted using a backing plate, as shown in Figure 2.2, in a single lap configuration. Heat input is estimated based on rotation speed, time, and plunge rate parameters, as well as the instrument load measurements torque (M_z) and axial force (P) and prescribed tool displacements plunge velocity (V_p) and rotation speed (ω).

$$Q = \int_0^t \frac{2\pi}{60}(\omega\, M_z)dt + \int_0^{t_p} P\, V_p dt \tag{11}$$

Using scanning electron microscopy (SEM), the bond length is recorded including regions of partial bonding. Figure 2.3 shows a diagram of the weld cross-section, and how the bond length was determined, while Figure 2.4 gives examples of partially bonded regions, where bonding was interrupted at the end of the weld process. Boundaries were determined once a clear transition from bonding to separation between the two sheets could be observed. Lap shear tests were also conducted to characterize the resulting joint strength for each of the processes after welding. A schematic of the lap shear test can be seen in Figure 2.5.

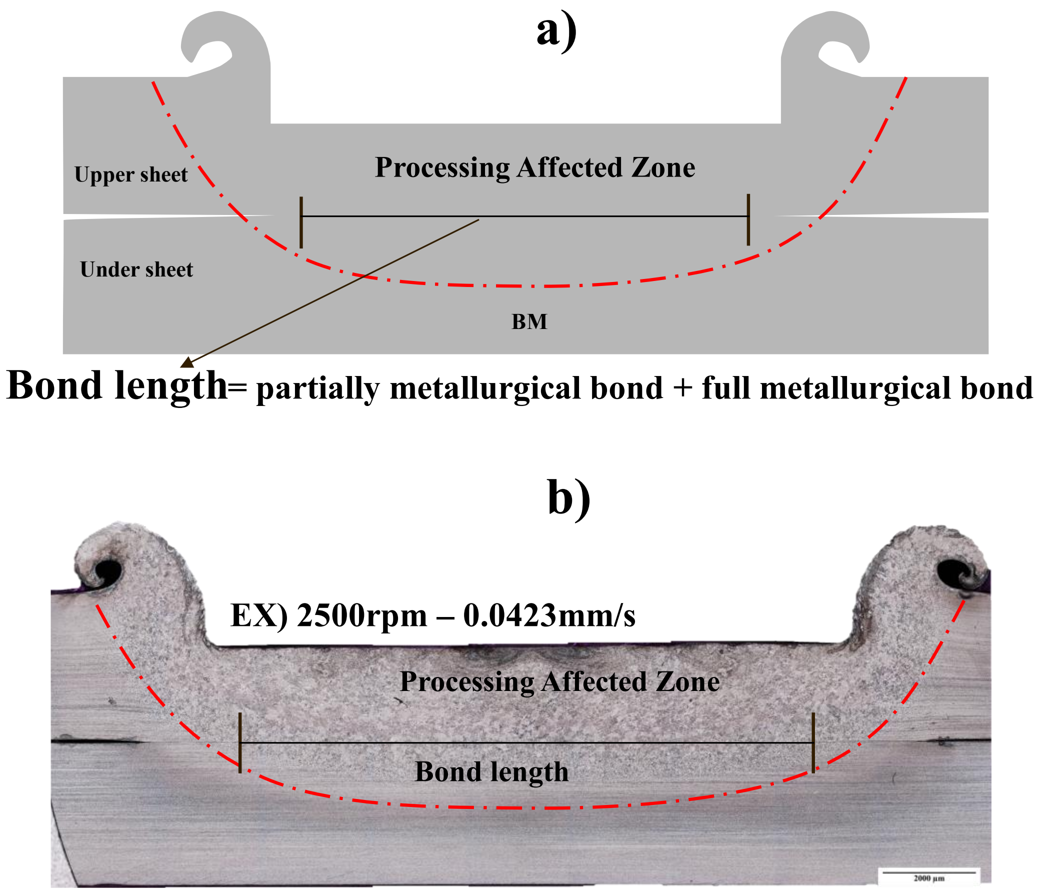

Figure 0.3 a) Cross-section of spot weld illustrating the bond length with respect to base metal (BM) and the friction stir processing zone b) Image of the weld cross-section showing the gap between the coupons transitioning to a bonding state

a)

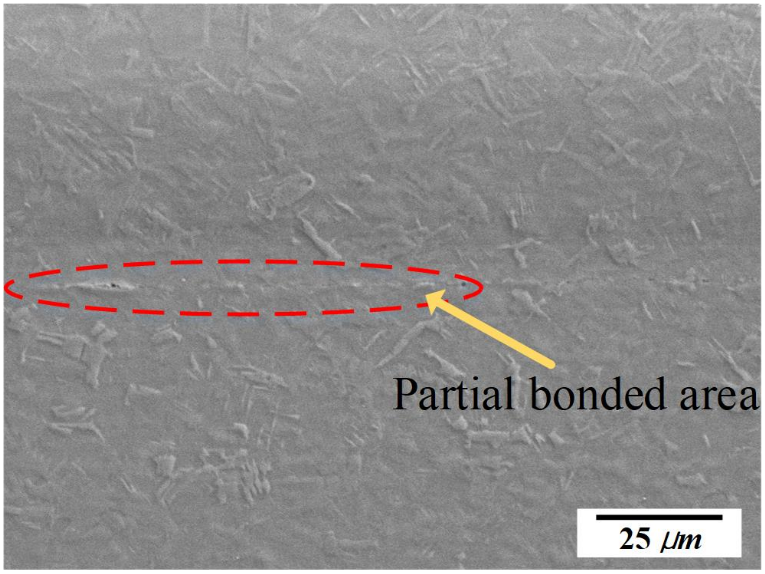

b)

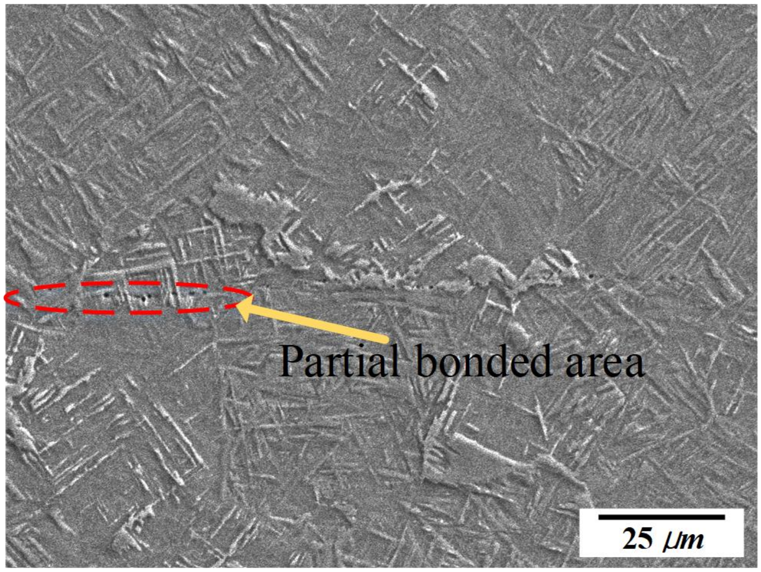

Figure 0.4 a,b) Examples where voids exists along the workpiece lap interface but the region has mostly transition to a bonded state

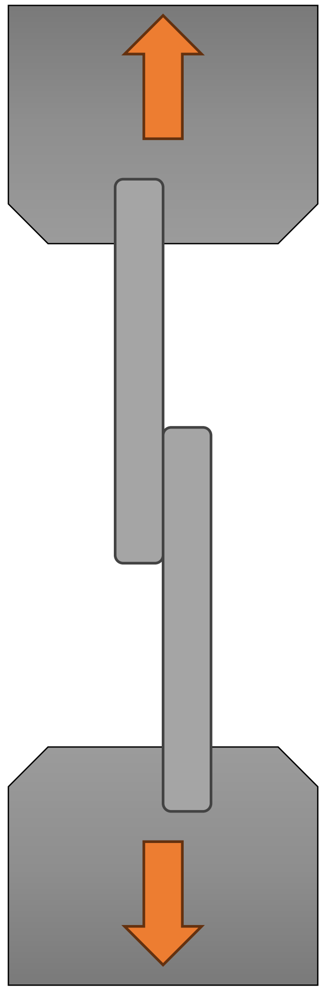

Figure 0.5 Schematic of lap shear test where the load cell grips the coupons and increases displacement at a constant rate, measuring the required load until the specimen fractures

2.3.2 CEL Analysis Setup

Using the CEL method in ABAQUS, a model was created to simulate each FSSW process. The volume of metal in the Eulerian domain represents the geometry of the overlapping layers (25.4 x 25.4 x 6.35 mm). The Lagrangian tool radius matches the radius of the tool used in the experiment (14mm). A reference point was defined on the axis of rotation of the tool. Displacements described by Table 2.1 are prescribed to the reference point. The tool is modeled as semi-analytically rigid. Because the backing plate and material constraints from the rest of the coupon, shear displacement at the surfaces is set as a boundary condition. Additionally, there are thermal boundary conditions that allow heat to conduct and radiate out of the system at a limited rate into a room temperature air bath.

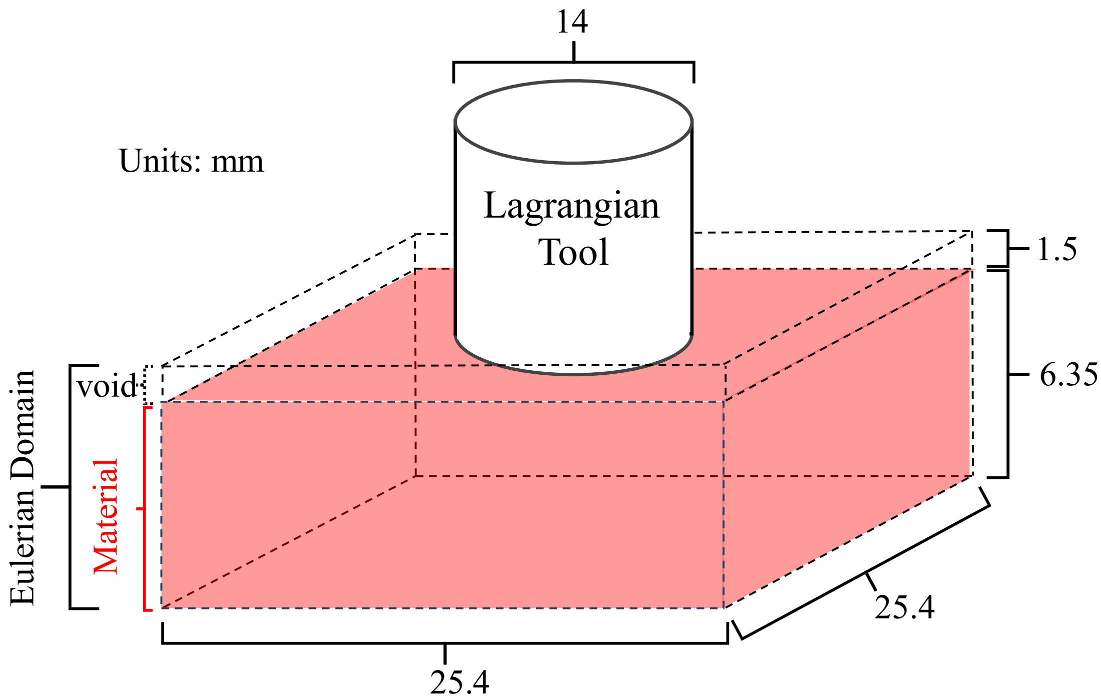

Figure 0.6 CEL assembly based on Ti64 experiments

Material parameters for the hyperbolic sine law are shown in Table 2.2 and were taken from literature [25].

Table 2.1: Hyperbolic Sine Creep Law Material Parameters

Material	**ln(A_n) (s^{-1})**	**σ_{ref} (MPa)**	**Q (kJ/mol)**	**n**	**R (J/mol-K)**
AA6061-T6	19.37	22.22	145	3.55	8.3145
Ti-6Al-4V	20.665	31.3	276	2.59	8.3145

The Hyperbolic Sine Creep Law was encoded within a user material subroutine (UMAT) to work with the iterative ABAQUS solver to calculate the deformation of Ti64.

2.3 FSSW Results and Discussion

2.3.1 CEL simulation excessive bonding

Initially, the simulations would inevitably terminate as deformation solutions began to exceed the speed of sound in at least one element. Reviewing the output database, some elements approached the melting temperature of Ti64 right before the model termination. The rotation speeds for the tool were reduced by an order of magnitude to increase the stability of the model. The solutions from the output database were used as inputs for the analytical bonding model (Eq. 8). Elements at the depth of the bonding interface were analyzed and showed unrealistic instantaneous bonding behavior as shown in Figure 2.7.

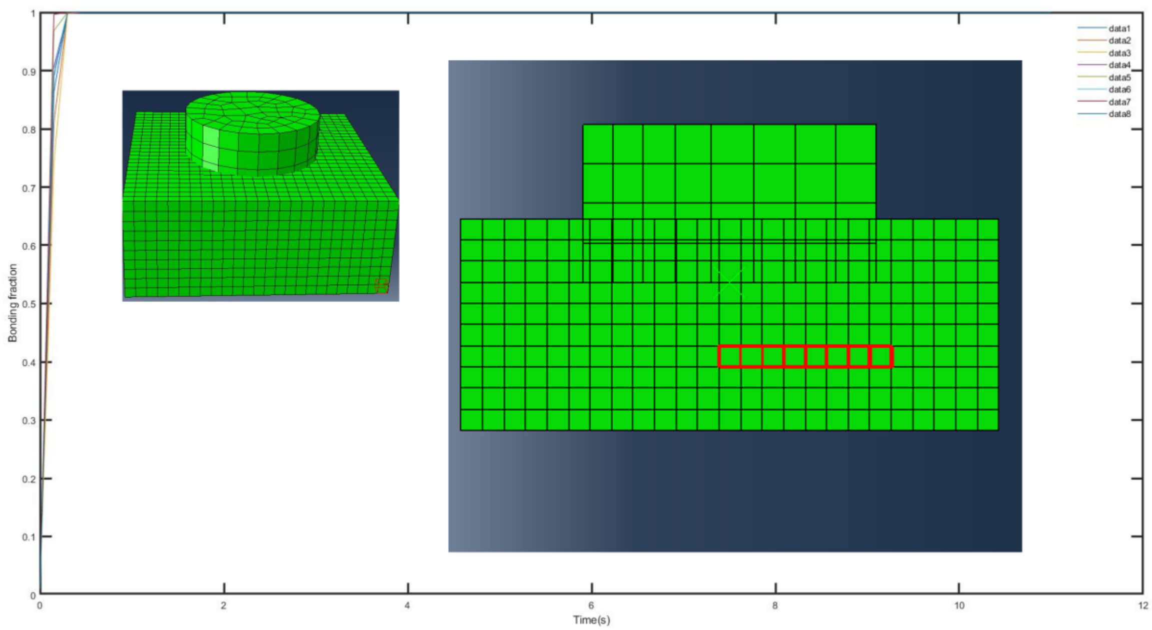

Figure 0.7 Coupled-Eulerian-Lagrangian (CEL) Assembly with reference point (RP) marked by the X and elements selected (red highlight) at the depth of the bonding interface and instantaneous bonding for each element seen in the bonding fraction dependent on time graph

The cause of the observed "melting" of Ti64 in the simulated solid-state process was unknown. The aluminum models previously studied [18-20] were shown to work well. Therefore, a spot weld was modeled using these same AA6061-T6 material parameters in ABAQUS and the UMAT. An assembly built for the aluminum process was also used where the tool size changed from 14 mm to 13 mm while the overall size of the Eulerian domain was increased from (25.5 x 25.5 x 6.35 mm) to (30 x 30 x 12 mm) as shown in Figure 2.8.

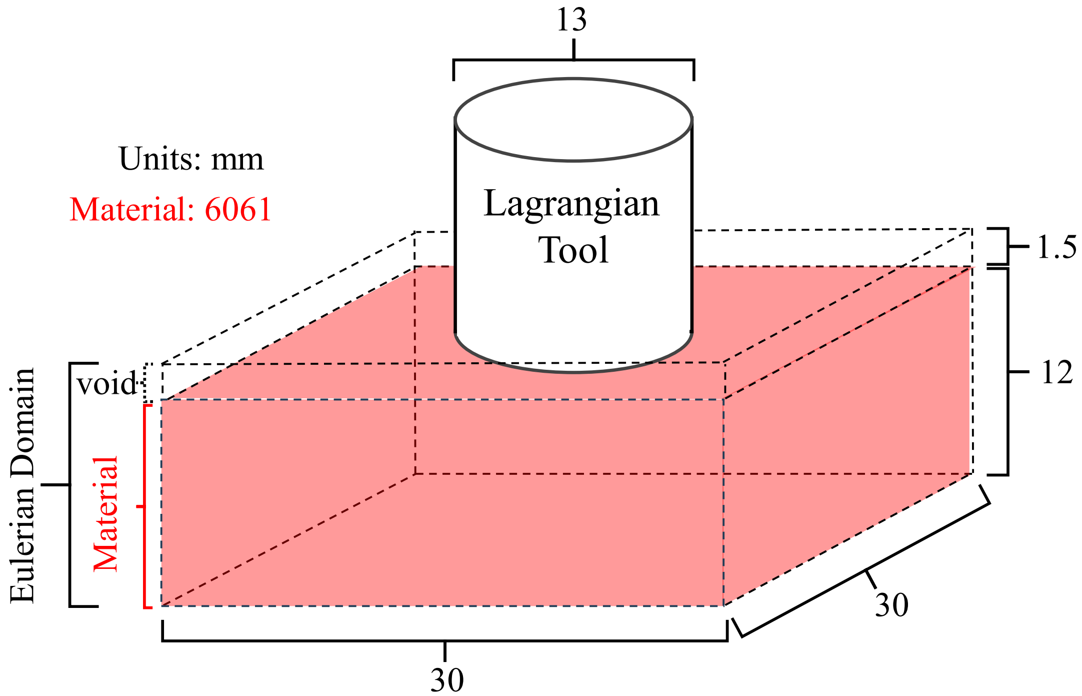

Figure 0.8 CEL assembly based on previous AA6061 modeling efforts

The rotation speed of the tool was set to 1000 RPM and the process time was reduced from twenty-one seconds, the max time resulting from the C3 process, to just half a second. The 3 mm depth lay parallel to the shoulder was analyzed. With the increased depth of the Eulerian domain, multiple layers were analyzed depth representative of the Ti64 experiments, including 6 mm and 12 mm. The depths, to scale with the assembly, can be seen in Figure 2.9. Under these conditions, the rate of bonding was retarded, enabling distinguishable patterns in bonding behavior to be studied. A criterion of 80% was set to represent the start of partial bonding. The 6 mm depth results are shown as an example in Figure 2.10. Each line represents the distance from the axis of rotation, not depth like in Figure 2.9.

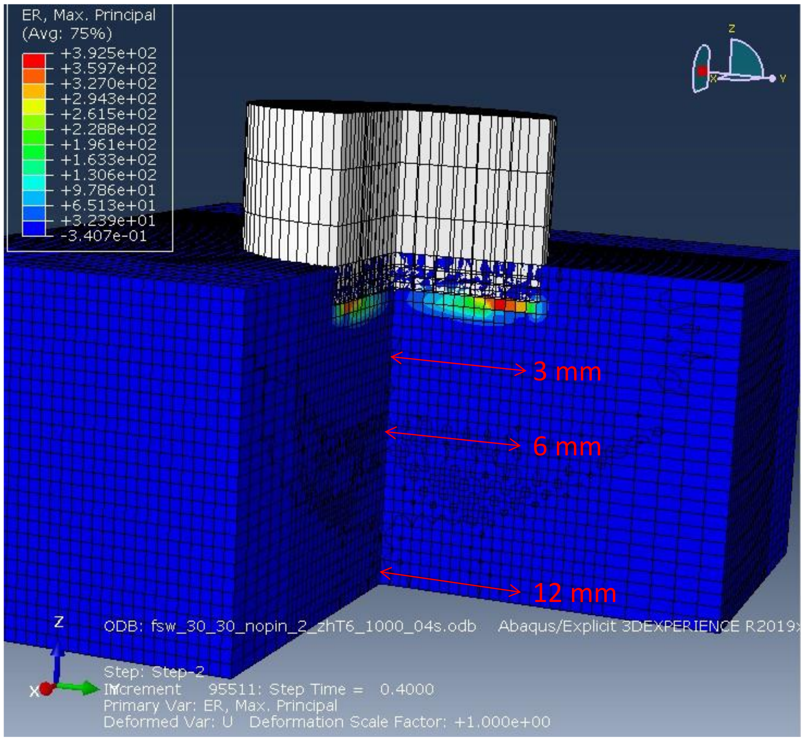

Figure 0.9 CEL assembly with depths analyzed by Sham-Needleman equation

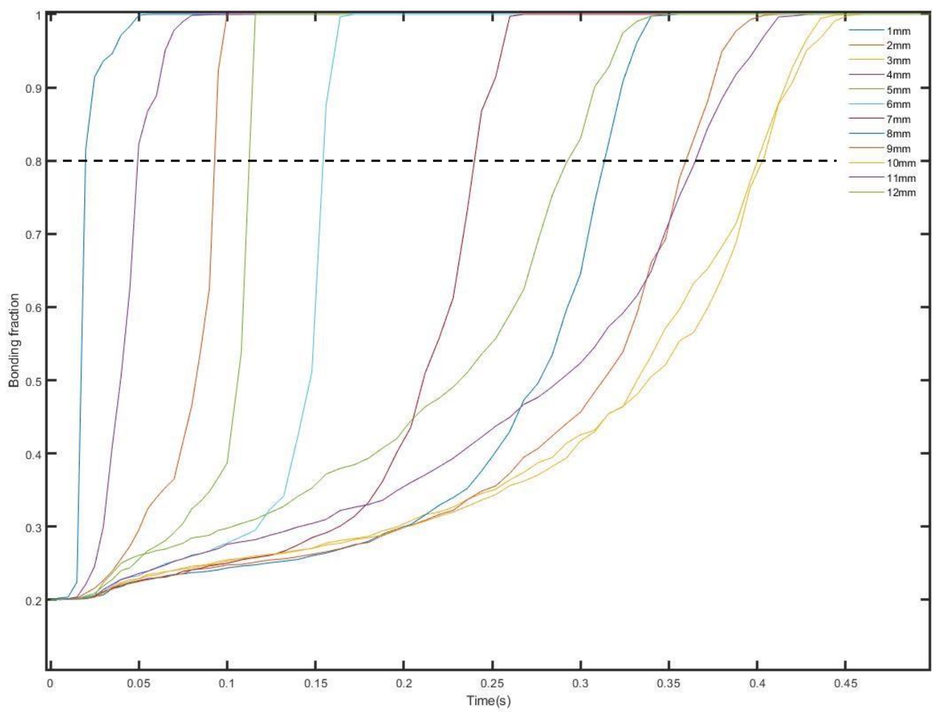

Figure 0.10 Extent of bonding dependent on time for 6mm depth. The dashed line represents when the transition to partially bonded occurs.

The change in internal energy of the model was calculated and recorded as a function of time by the ABAQUS solver. Elements were selected to represent the bond length observed by SEM for each process as a percentage of the tool radius. For each depth level (3 mm, 6 mm, and 12 mm), the extent of bonding was tracked for each element. The results are shown in Figure 2.11. Just the 6 mm results are compared to the experimental results in Figure 2.12. Qualitatively, the same behavior occurs. Initially, bond length is limited to smaller values; a sudden growth occurs, followed by a plateau at a value slightly less than the length of the tool. The asymptotic behavior was also predicted based on the previous FSW efforts, which led to the development of a process window.

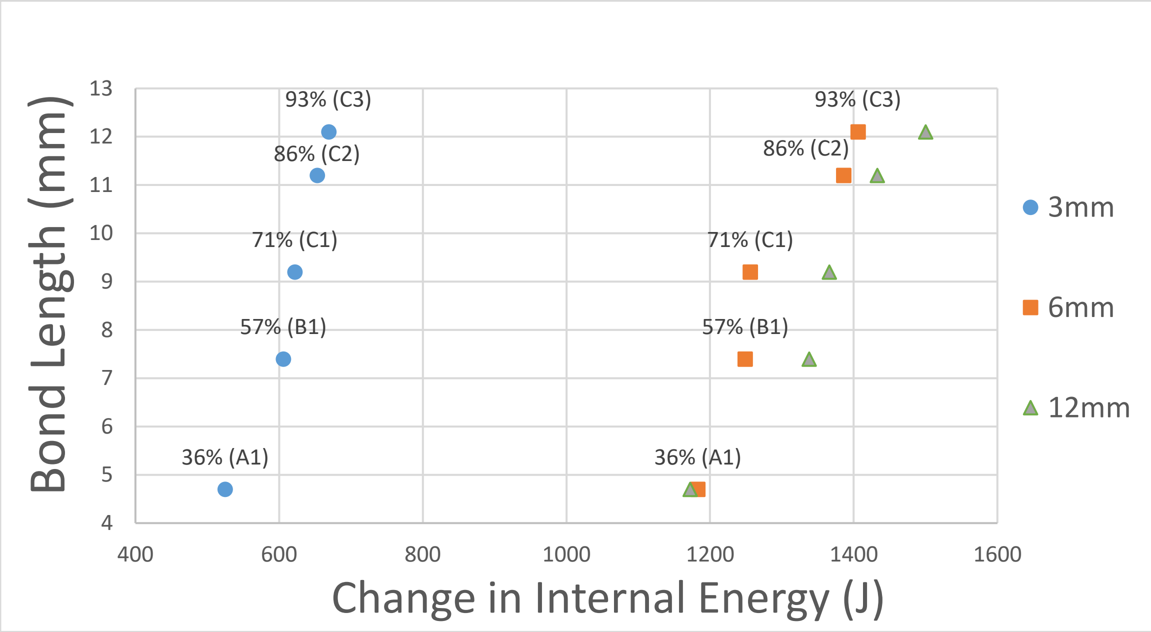

Figure 0.11 Graph plotting when recorded 0.8 criterion was achieved by each element in terms of change in internal energy

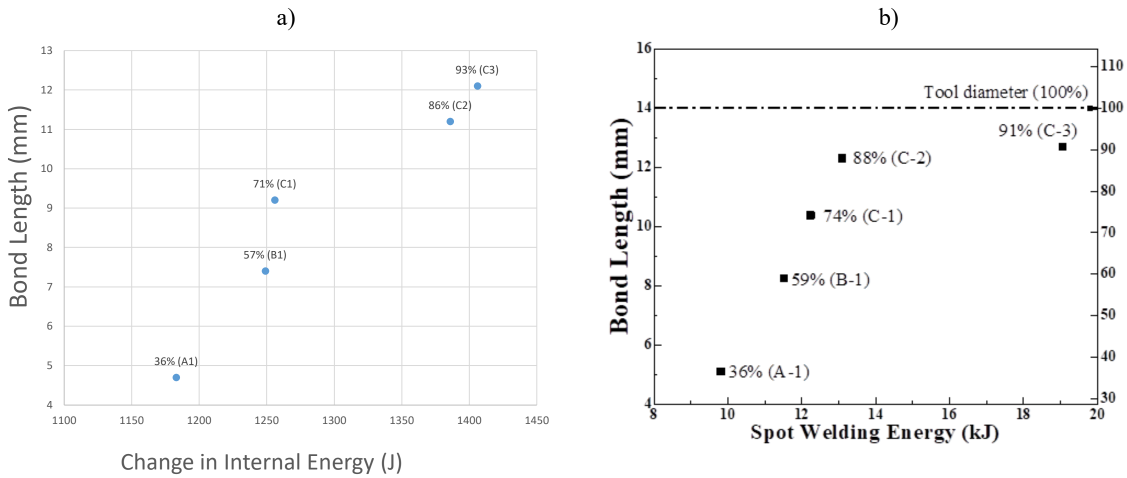

Figure 0.12 Extent of bonding dependent on input energy for a) 6mm depth numerical solution and b) empirical solution

2.3.2 Developing FSW process windows

An appealing feature of FSW is the retention of microstructural features due to solid-state processing. To improve performance, bonding should be maximized while microstructure evolution minimized. However, extreme deformation occurs at elevated temperatures, so microstructure evolution is inevitable in FSW, but the degree can vary. The difficulty of process optimization is trying to balance maximizing bond length with minimizing temperature and deformation. Wang [20] and Panda [26] offer similar process windows, as shown in Figure 2.13. Wang's window is based on the analytical solution for the Sham-Needleman equations based on process parameters. Panda conducted multiple FSW of overlapping plates varying multiple parameters. Plates were machined into lap coupons and mechanical tests were conducted. Hypersurfaces were constructed in the parameter space by fitting relationships between multiple parameters and UTS. Empirical solutions require multiple welds and mechanical tests. Although this provides insight into the relative behavior, if other parameters besides process are changed (plate thickness, material, etc.) then predictive equations can no longer be used. Mechanism-based solutions can unite understanding between material, geometry, and process.

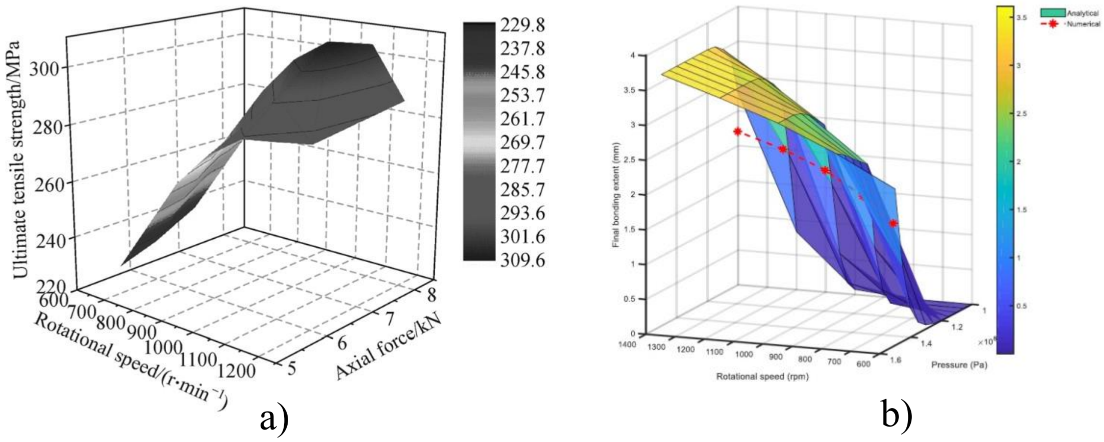

Figure 0.13 Normal loading and rotational displacement dependent process windows for AA6061 FSW a) ultimate tensile strength in lap shear tests [26] b) extent of bonding [20]

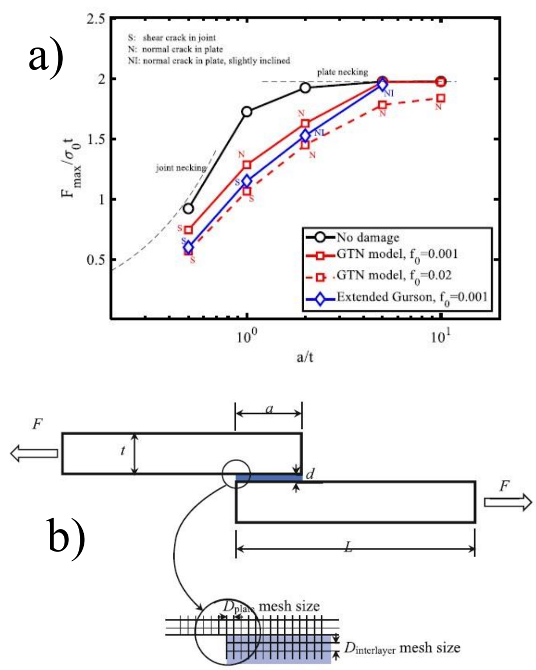

Figure 0.14 2D model for lap shear testing [27] a) UTS normalized by yield strength and coupon thickness compared to bond length normalized by coupon thickness b) Schematic of geometric parameters and lap shear test

The qualitative similarity of ultimate tensile strength (UTS) is unsurprising as the relationship between bond length and lap shear strength has been demonstrated [27]. As shown in Figure 2.14, as the bond length increases the lap shear results from the Ti64 FSSW (Figure 2.15) were plotted in a similar dimensionless form, as shown in Figure 2.16. The cross-sectional area was used to normalize the force over stress term.

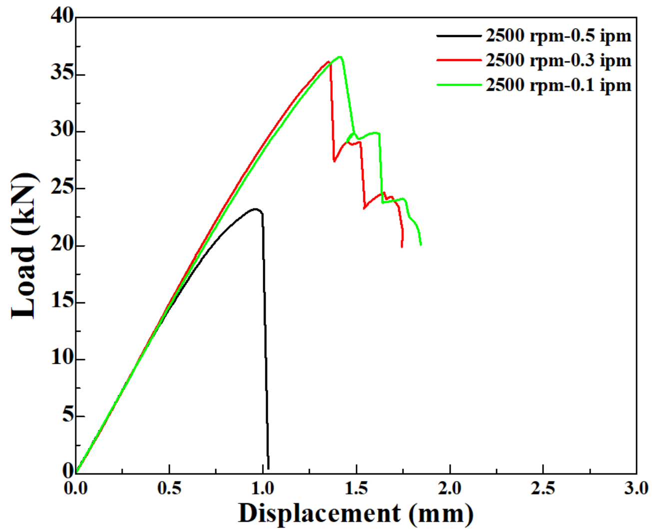

Figure 0.15 Lap Shear tests on processes C_{1-3}

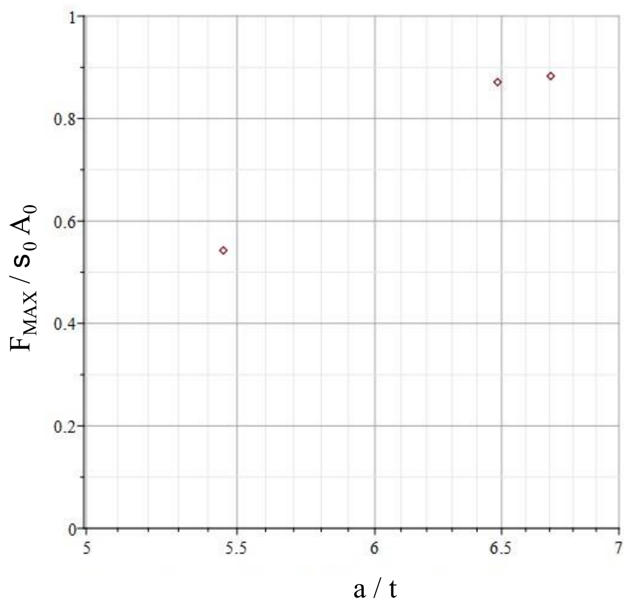

Figure 0.16 Normalized UTS compared to normalized bond length for Ti64 FSSW data

A similar asymptotic relationship is observed, although UTS convergence occurs at 1 rather than 2. This can be explained by a violation of the 2D symmetric assumption. This would be valid under the FSW coupons, but not for FSSW. As shown in Figure 2.17, for the FSW lap coupons, the tool traverses resulting in a solid line of weld material, while FSSW results in a round weld nugget.

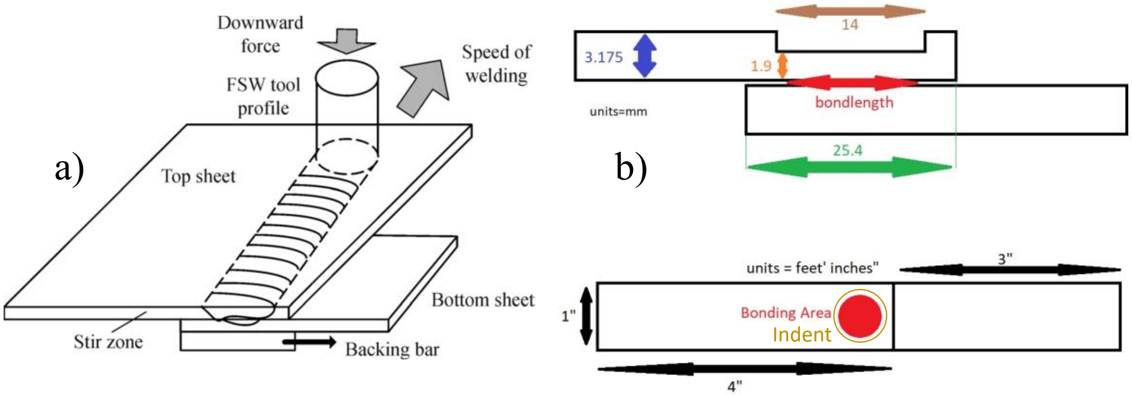

Figure 0.17 Differences in a) FSW and b) FSSW coupons

The introduction of the indentation and the variation of bond width across the coupon create regions where stress can concentrate. This is seen in the failure modes of the samples. Rather than failing due to necking of the joint or plate, nugget pullout or brittle plate cracking were observed. Partial bonding regions would also act as preexisting damage that would shift the curve down as defects provide a path for cracking.

2.3.3 Investigation of excessive heat in CEL simulation

An attempt was made to understand why the Ti64 simulations resulting in "melting." Using the aluminum displacement controls and assembly geometry from Section 2.3.1, Ti64 material properties were reintroduced, and results were compared. The thermal conductivity of AA6061 is around 170 W/m·K while Ti64 is around 7 W/m·K. Figure 2.18 shows how heat becomes trapped under the tool. However, Ti64 does not melt in practice despite the low thermal conductivity. Therefore, the model must be missing some aspect that is not being accounted for.

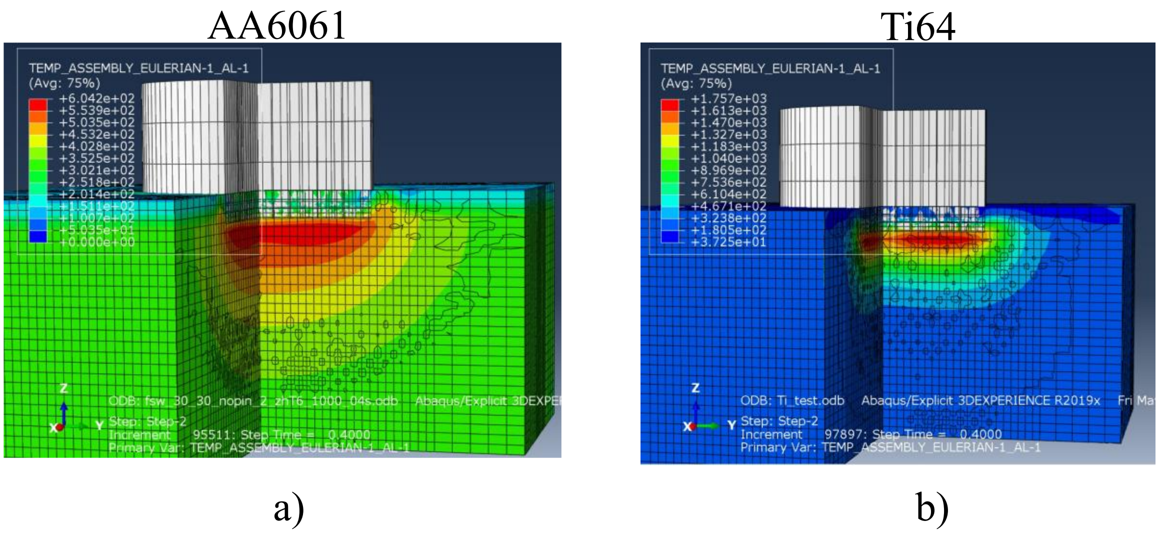

Figure 0.18 CEL start of dwell step after initial plunge a) AA6061 b) Ti64

Another hypothesis was that the constitutive model was allowing for higher degrees of plastic deformation, resulting in the high temperature and bonding values. However, after evaluating isotherms on a deformation map, the creep rate of AA6061 is higher than Ti64 under all conditions.

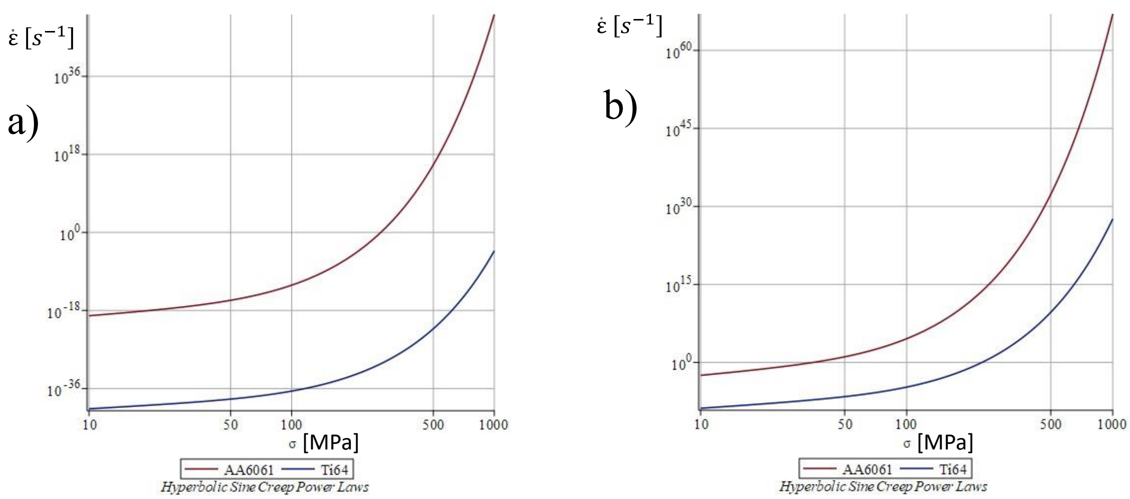

Figure 0.19 Creep rates relative to applied stress a) Room Temperature b) T = 600ºC

An alternative explanation is machine compliance. The plunge depths are relatively small on the mm scale, while the spindle of the weld unit is long. It was proposed that because, in the simulation, a semi-analytical rigid tool was used, the true depth of the plunge was less. ABAQUS will apply whatever load necessary to obtain the target, greatly increasing friction and therefore torque to maintain rotational displacement as well. This provides a feedback loop causing a temperature spike. The target depth was reduced by increments of one order of magnitude up to one one-thousandth of the original target. In figure 2.20, results showed values converging to the experimental estimations. As the simulation time increased (i.e. $C_1 \rightarrow C_2$), the numerical and analytical solutions diverged with the analytical solution staying truer to the experimental data. Data is missing due to simulations being interrupted.

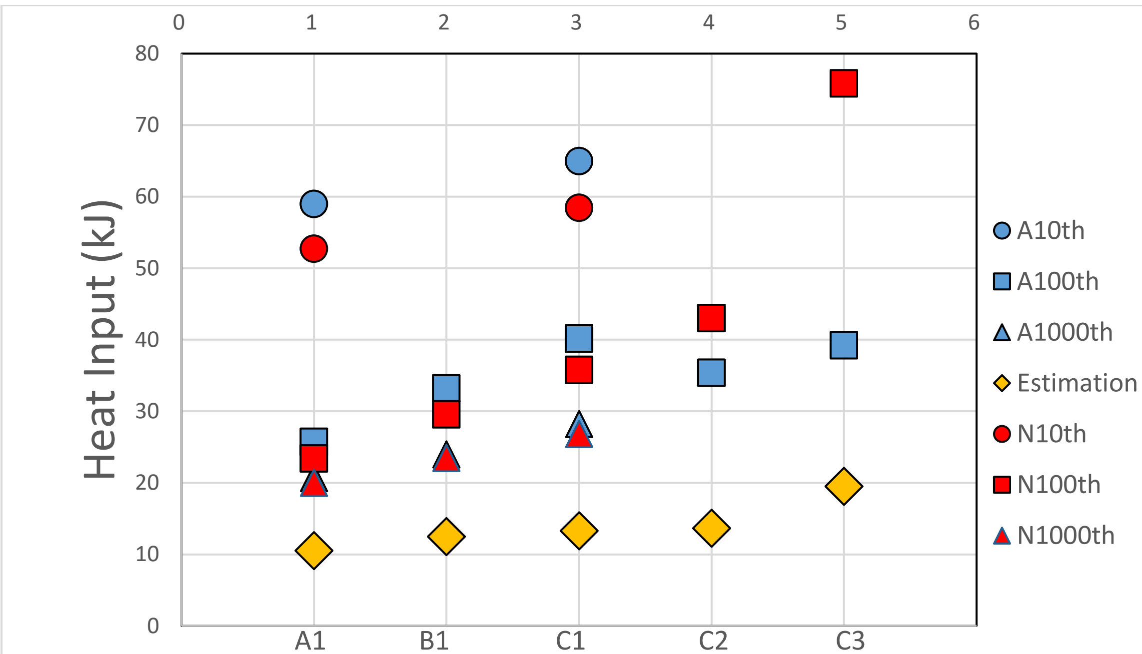

Figure 0.20 Various depth reductions compared to the original estimations based on experimental data (yellow). Analytical solution based on Eq.7 (blue). A numerical estimation was made in ABAQUS based on change in internal energy of the system (red).

2.4 Conclusions

Previous work demonstrated how process windows can be constructed for FSW of AA6061 based on an ICWE framework that explained and quantified how heat is generated and the mechanisms for bonding occur in FSPs, while a CEL method can be used to simulate the thermomechanics. Experimental efforts were used to validate these models using FSSW of Ti64. Initially, the CEL model used to supply data for analytical solutions could not be executed and the material properties of Ti64 were identified as a contributing factor. Additional changes included a butt to lap weld configuration and the elimination of tool travel to produce a spot weld. Asymptotic bonding behavior was shown when analyzing a lap interface of a spot weld using AA6061 properties. By comparing the results to the bonding behavior measured by microscopy, the CEL method for analyzing a lap spot weld was demonstrated. The reintroduction of Ti64 properties required rethinking the model setup. By reducing the plunge depth, the predicted heat generation based on the analytical model aligned with the experimental estimation.

Models should be versatile to be valuable. While the mechanism-based analytical methods appear to hold true, the material changes introduce challenges for the numerical methods. Further work is required for the CEL setup to make quantitative predictions for Ti64. While changing the displacement controls led to significantly improved performance, other aspects like thermal conductivity and workability make Ti64 a more challenging alloy to model. The domain size was increased to separate the interacting surfaces from boundary conditions, stabilizing mechanical fields. However, these boundaries provided an outlet for heat to escape. Refining either the boundary conditions, the surface interactions, or both could resolve this issue. Additionally, the use of rigid properties can aid in reducing computation costs, but can cause unforeseen consequences.

Chapter 3

Analytical Solution to Printing Temperatures in AFSD

The experimental work for the following chapter was performed by Dr. Joshua Kincaid and Mr. Elijah Charles under the advisement of Prof. Tony Schmitz from the Department of Mechanical Engineering. The experimental dataset was provided by Prof. Schmitz's group. Experiments were also conducted with Prof. Tony Zhongshun Shi from the Department of Industrial & Systems Engineering [36]. A final version of this chapter is currently being submitted for publication.

3.1 Introduction

3.1.1 Preface

Similarities between FSW and AFSD suggest that an ICWE framework could be assembled by building on the foundation laid by the FSW ICWE framework outlined in Chapter 2. Additionally, long-established theory of fusion welding can be applied to an AFSD ICWE framework such as steady-state temperature field solutions. There are still differences between AM and welding processes. For example, while welding typically involves applying a heat source along adjoining surfaces once, the layer-by-layer approach in AM will result in thermal cycling. The goal of minimizing microstructure evolution while maximizing bonding at the same time has somewhat contradictory requirements. Understanding the links between print parameters, heat generation, temperature, build geometry, microstructure, and performance is necessary for print optimization. Using the FSW heat generation model established by Wang [19] combined the Rosenthal solution [28] could be used to predict printing temperatures.

3.1.2 Literature Review of AFSD

Ideally, wrought material could be used as feedstock and property retention could be achieved due to the solid-state processing while simultaneously printing fully dense parts. Though precipitate-strengthened aluminum alloy systems used in the aerospace industry show a drop in yield strength and ultimate tensile strength when undergoing an AFSD process, attributed to precipitate kinetics at the elevated temperatures [29,30]. The drop in strength seems unavoidable, however ductility has been shown to fluctuate. Contrary to a traditional strength-ductility tradeoff, rupture strain of printed material can be both lower and higher when compared to wrought material. Ductility drops are especially common when conducting uniaxial tensile tests perpendicular to the in-plane layers or the build direction (BD). To better understand relationships between printing parameters and print material performance, parametric studies are conducted. The variables rotation speed (ω) and travel speed (V) influence both heat generation and strain rates. Contamination from lubrication of the feedstock has been attributed to defects at bonding surfaces, resulting in anisotropic behavior [31-33]. Hoarston [33] observed that the lubricant suppresses metallic bonding resulting in micro-voids and demonstrated that by combing deposition pitch (the ratio of travel speed and spin velocity: ω / V) and heat input into a single variable called heat pitch, a criterion for sufficient bonding can be defined. Hoarston's criteria indicates the importance of a deeper understanding of the relationship between printing parameters and heat input for developing process models that can aid in process optimization. An empirical power law is proposed by Garcia [34] to relate ω and V to the peak printing temperature. This relationship is reasonable as these parametric terms determine the relative velocity of the friction surfaces and V determines the speed of the heat source. Building off this work, Griffiths [35] proposes a simple process window for printing fully dense parts based on heat increasing as ω increases or V decreases; see Figure 3.1.a.

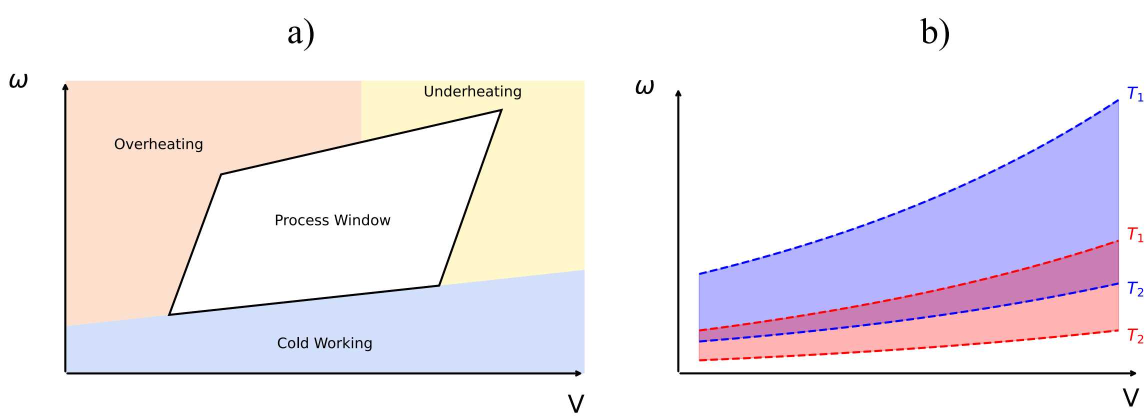

Figure 0.1 AFSD proposed process windows a) Sufficient and insufficient heat argument b) Isotherm approach

Leaving the optimal range results in melting or material damage from overheating, insufficient bonding from underheating, or interruptions of seamless deposition of the feedstock in either case. Our process window can be seen in Figure 3.1.b with similar overheating and underheating concerns. This approach assumes that under constant heat input, as well as other process and material parameters, isotherms can be plotted on the same process map. However, a thorough understanding of how to determine heat input is required to make a quantitative argument.

The ω / V ratio and its relationship to heat generation and total strain are important for understanding microstructure evolution and bonding behavior for both processes. Mechanical properties are therefore influenced by these variables. For welding processes, a point of concern is the base metal, HAZ, and weld metal microstructure gradient. The variation in properties creates mismatch in behavior that in some cases leads to failure. In AFSD, the resulting structure is entirely friction stir processed, but the AM method still results in property mismatch. The layer-by-layer approach in AM will result in thermal cycling. The goal of minimizing microstructure evolution while maximizing bonding contains somewhat contradictory requirements. Understanding the links between print parameters, heat generation, temperature, build geometry, microstructure, and performance is necessary for print optimization. While relative velocity, determined by ω and V, is certainly an important feature in heat generation in friction processes, traction forces of interacting surfaces are also crucial for determining heating from friction and plastic deformation. Based on our understanding of FSW, the applied load and torque should be considered in addition to other AFSD processing parameters and material properties to predict heat generation. A parametric study will be conducted and analyzed under the assumption that the thermomechanical reasoning for heat generation in FSW is analogous to AFSD. Confidence in this assumption can be demonstrated through agreement between the theory and experimental results and would indicate other FSW process models could be used to in process advancement.

3.2 Experimental Method and Results

A parametric study was performed using fixed displacement controls. A simple wall shape was built following an 8” (203.2 mm) straight track in the x-direction. The height (z) of the wall was roughly 2” (50.8 mm) and was 30 layers thick. The AFSD MELD L3 model was used which is a commercial AFSD unit. The L3 is designed for a smaller footprint with a build volume of 45 in x 23 in x 23 in (114.3 cm x 58.4 cm x 58.4 cm) and optimized for solid bar feedstock. Wrought AA7075-T6 was the feedstock and substrate material. Three speeds were investigated: 135, 115, and 105 RPM. However, the loading of the system was upgraded midway through the experiment, and the tool bore and material were altered to accommodate this change. The tool for the 135 and 115 prints used a 3/8" (9.53 mm) square bore tool made of H13 tool steel while the new tool was made of a Cu-Be alloy with a 1/2" (12.7 mm) bore. The travel velocity was 5 in/min (2.12 mm/s) and the feed rate was 4.55 in/min (1.9 mm/s). Torque values recorded by the L3 unit are estimated from the applied torque. Printing temperatures are measured from the embedded thermocouple in the tool and assumed to be close to peak temperatures. The system is manually loaded. Each layer that did not require loading included a two-minute pause to simulate reloading. Data is continuously collected by the AFSD unit. To isolate stretches of steady state for each pass, certain conditionals were set for feed rate, spindle speed, feed load, travel velocity, and tool torque. The criteria does not necessarily include all travel data and therefore each pass data set varies slightly in set size. It is hypothesized that torque and rotation speed should be proportional to the heat generation rate and therefore the measured tool temperature.

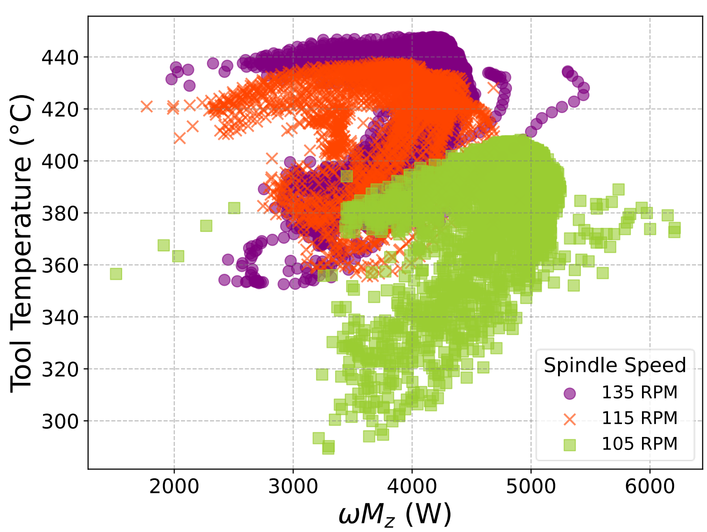

Figure 0.2 Temperature dependence on power for all three speeds showing the formation of the "7" curve

These variables are plotted in Figure 3.2. If proportionality is expected, then a linear relationship should be observed. However, two linear regions form resembling a 7-numeral shape. As shown in Figure 3.3, the "7" curve maintains its shape while drifting to higher temperatures and lower torque values. Additionally, each pass starts at the base of the seven, finishing the end of the upper linear region. To investigate deviatory behavior, a method of relating heat input to temperature is required.

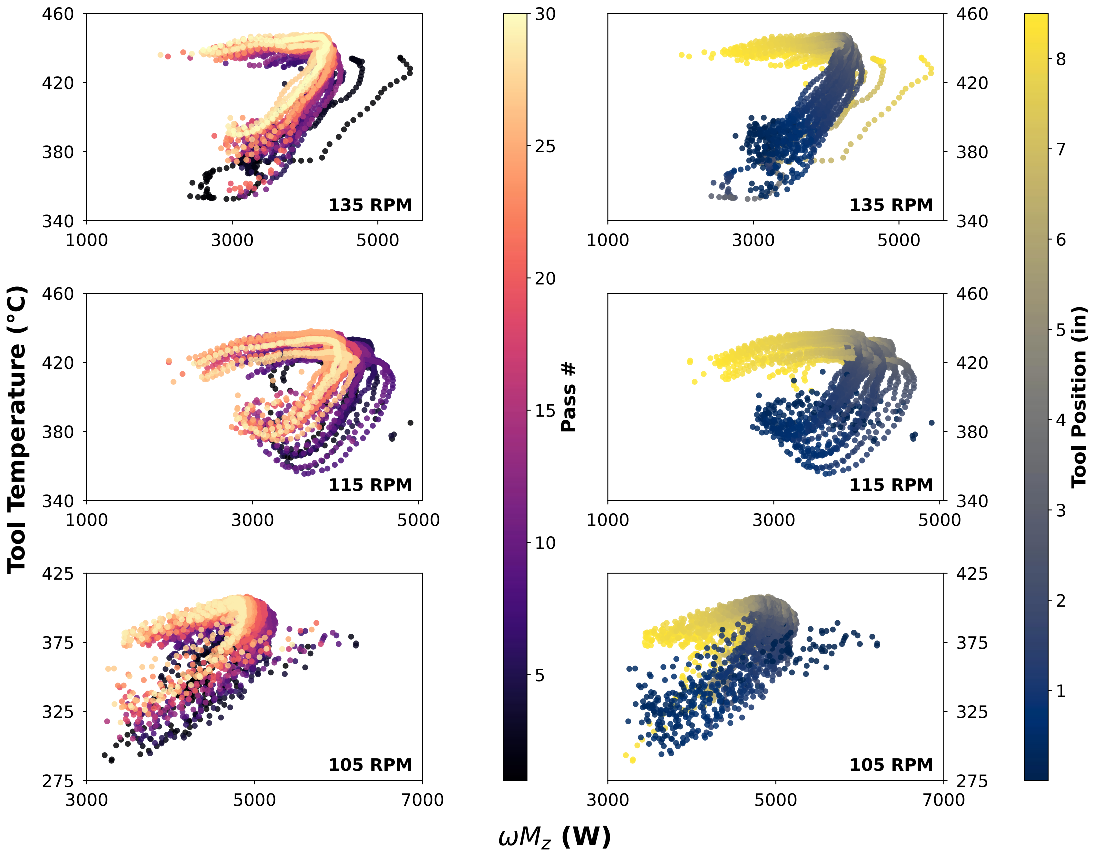

Figure 0.3 "7" curve plotted with different speeds and color axes denoting the pass number and tool position

3.3 Modeling the Thermomechanical Responses

In welding, a common method of modeling steady-state temperature fields is the use of the Rosenthal Solution. The model assumes the heat source is traveling at a constant rate and outputting heat at a constant rate along a half-plane, material properties are temperature independent, and that heat loss at surfaces due to convection is negligible while heat transfer in the half-space are purely conductive. The Rosenthal model is described by Equation 12.

$$T(x, R) = T_0 + \frac{Q}{2\pi k}\left(\frac{1}{R}\right) e^{-\frac{V_x}{2\alpha}(R-x)} \tag{12}$$

The ambient temperature is represented by T_0 and T is the temperature at a given location. R is the distance from the heat source. There is asymmetry in the travel direction (x) with the degree dependent on the travel velocity (V_x). The constant material properties used are thermal conductivity (k), density, and specific heat. All three compose thermal diffusivity ($\alpha = \frac{k}{\rho\, C_p}$). Based on previous FSW modeling results, temperature and strains are highest near the interacting surfaces. However, while strain rates vary significantly across this area, the temperature is uniform. Additionally, the AFSD tool has an embedded thermocouple near the edge of the tool. As mentioned, it is used to monitor the temperature and can be assumed to be a rough estimate of the peak temperature. A modified version of the Rosenthal Solution was derived assuming that the heat source is circular area under the tool (with radius a) instead of a point and the heat generation rate from FSW.

$$T_{max} = T_0 + \frac{\omega M_z}{2\pi k a} \tag{13}$$

Equation 13 can also be written in a dimensionless form where C_1 is a dimensionless parameter.

$$\frac{T_{measured} - T_{RT}}{T_{RT}} = C_1 \frac{\omega M_z}{T_{RT}\ k\ a} \tag{14}$$

By plotting the relationship described by Equation 14 in Figure 3.4, the slope of the relationship can be used to solve for the constant C_1. Because the relationship is dimensionless, this constant should be around 1. The upper region of the “7” represents additional heat near the end of the print that is unaccounted for by the model.

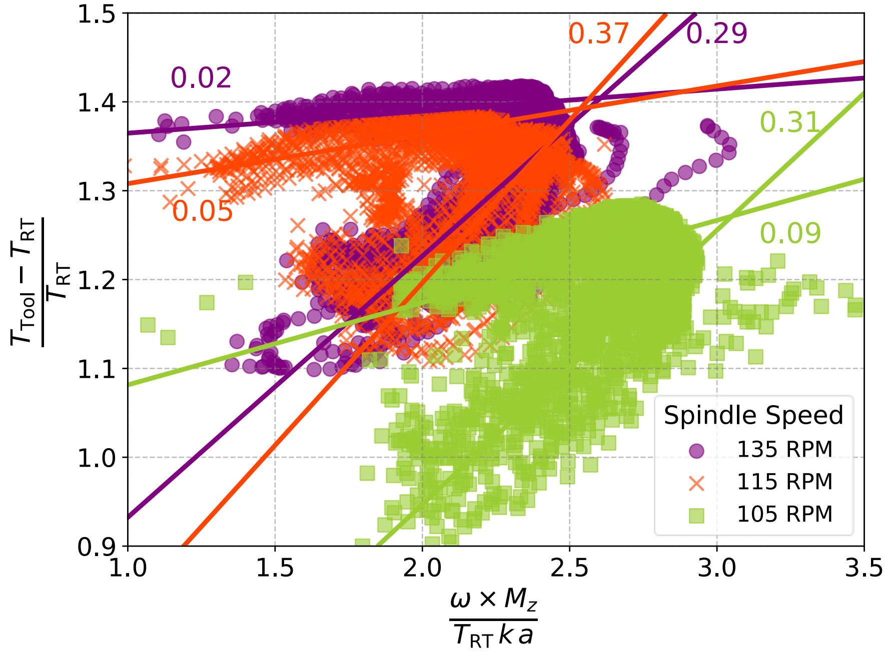

Figure 0.4 Temperature dependence on power for all three speeds plotted in dimensionless form to solve for C_1

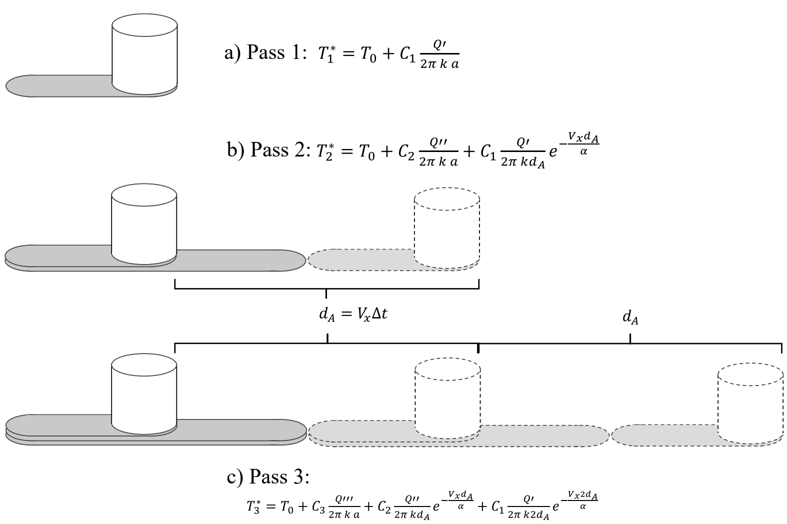

Figure 0.5 Superimposing temperature fields from each previous pass a) First pass, b) Second pass, and c) Third pass solutions

The first couple of passes show a single linear region (i.e. the second upper region linearity is minimal). One hypothesis was that previous passes contributed to this additional heat. The temperature solution omitted the travel term from the Rosenthal Solution because initially a full field representation was not being attempted to be solved. However, if each pass is modeled as a separate heat source sequentially traveling at the same location at different times, like in Figure 3.5, this term becomes important in determining the contribution of the heat wake left behind each heat source. Equation 15 superimposes temperature fields treating each pass like multiple heat sources traveling through the same space and separated by a distance based on the travel speed of the tool and the average time between each pass.

$$T_n = T_0 + C_n \frac{Q^{(n)}}{2\pi\, k\, a} + \sum_{j=1}^{n-1} C_{n-j} \frac{Q^{(n-j)}}{2\pi\, k\, j\, d_A} e^{-\frac{V_x\, j\, d_A}{\alpha}} \tag{15}$$

Equation 16 shows the max contribution by solving infinite passes at steady power input.

$$\frac{Q}{2\pi\, k\, d_A} \sum_{j=1}^{\infty} \frac{e^{-\frac{V_x\, j\, d_A}{\alpha}}}{j} = \frac{Q}{2\pi\, k\, d_A} \left[-\,ln \left(1 - e^{-\frac{V_x d_A}{\alpha}} \right) \right] \tag{16}$$

By assuming power input of 2500 watts and all C constants are equal to 1, the infinite-pass contribution was shown to be negligible. Although this modification to the model did not explain the upper region of the “7” curve, the system did not return to ambient temperature after each pass. The drift correlated with the pass number in Figure 3.3 could be explained by an increasing reference temperature.

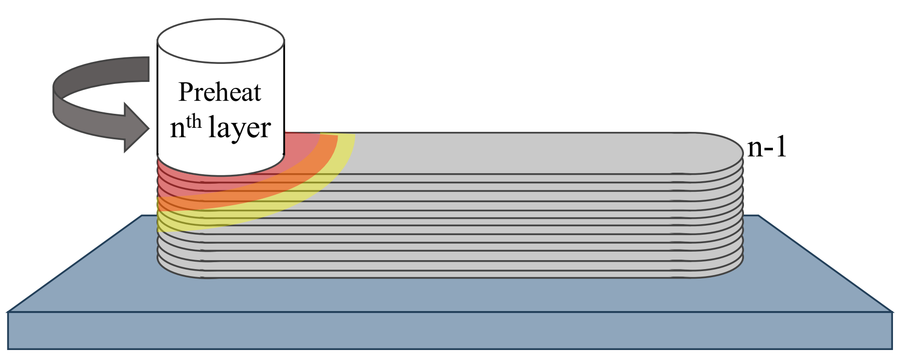

Figure 0.6 Spinning tool generating heat during the dwell prior to the travel step

Before deposition, the tool must preheat to plasticize the feedstock. During this step, the tool does not travel while heat is released into the system, as shown in Figure 3.6. To address a static heat source, Green's function [37] is used to model the temperature field. The function defines a transient heat source in a half-space.

$$T - T_0 = \frac{q * e^{(-R/4\alpha t)}}{\rho\, C_p\, 4\, (\alpha \pi t)^{3/2}} \tag{17}$$

Lower case q refers to energy rather than the earlier used upper case Q power. The total energy input prior to steady state travel was estimated by integrating the power estimation from Equation 5 over the total time. Typically, the preheat process would produce around 500 kJ of energy. Assuming density (ρ), specific heat capacity (C_p), and thermal diffusivity (α) are temperature independent, all constants can be described by perfector A and Equation 17 can be rewritten as Equation 18. Like in the modified Rosenthal solution, radius R will be represented as the radius of the tool a, and t is time.

$$\Delta T(t) = A\, t^{-3/2}\, e^{(-a/4\alpha t)} \tag{18}$$

Determining for the maximum change in temperature (ΔT_{max}) for each location ($x > 0$) and the time this occurs (t^*) can be calculated by solving Equation 19.

$$\frac{\partial \Delta T}{\partial t} = A\, e^{(-a/4\alpha t)}\;\; t^{-7/2} \left(\frac{a}{4\alpha} - \frac{3}{2} t\right) = 0 \tag{19}$$

$$t^* = \frac{a}{6\,\alpha} \tag{20}$$

$$\Delta T_{max} = A\, \left(\frac{a\, e}{6\, \alpha}\right)^{-3/2} \tag{21}$$

Solving the Green's function peak temperature, as shown in Figure 3.7, again shows negligible temperature contributions that peak after the tool has passed.

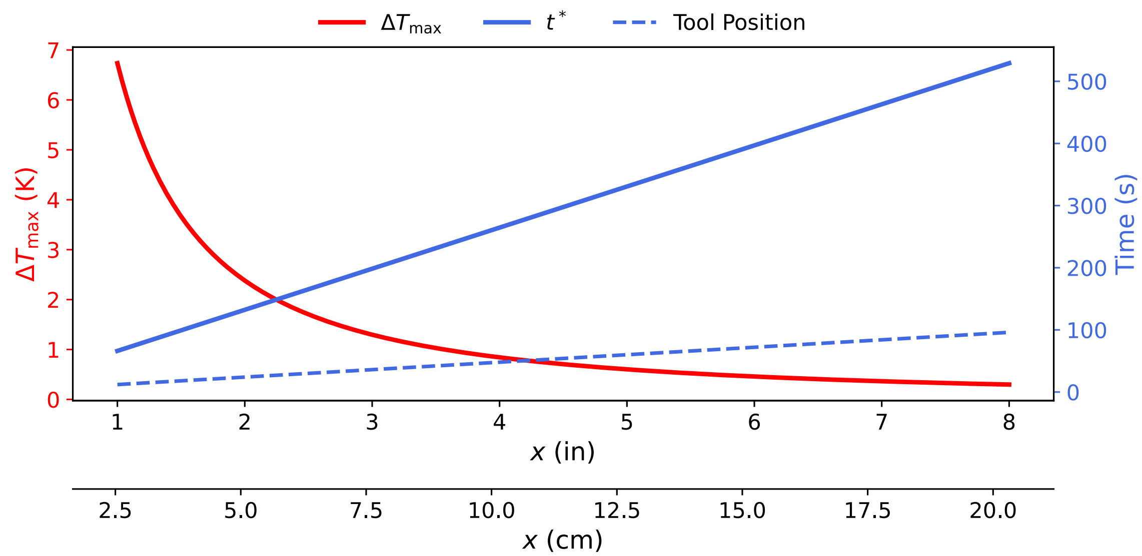

Figure 0.7 Transient heat source solution where peak temperature is plotted in red from the front edge of the tool to the end of the track. Time the peak occurs is plotted blue with the position of the tool plotted as a dashed line.

With each pass, a new boundary becomes more prominent, hindering conduction. The system the heat source interacts with transitions from a flat surface like the substrate to the wall being built. Equation 23 reintroduces the travel term to the Rosenthal solution plus an additional heat term based on a geometric argument of the thinning of the half-space to a semi-infinite wall in increments of width W.

$$\Delta T_{Rosenthal} = \frac{\omega M_z}{2\pi k a} e^{-\frac{V_x a}{\alpha}} \tag{23}$$

$$\Delta T = \Delta T_{Rosenthal} + \Delta T_{Additional} = \Delta T_{Rosenthal}(1 + \xi) \tag{24}$$

Where,

$$\xi = \frac{\Delta T_{Additional}}{\Delta T_{Rosenthal}} = \frac{Va}{\alpha} e^{\frac{Va}{\alpha}} \sum_{m=1}^{\infty} \frac{e^{-\frac{Va}{\alpha}\frac{W}{a}m}}{\frac{Va}{\alpha}\frac{W}{a}m} \tag{25}$$

This can be approximated in the case the wall thickness equals the diameter of the tool (m=1).

$$\Delta T = \Delta T_{Rosenthal}\left[2 + \frac{3}{2}e^{-\frac{7Va}{4\,\alpha}}\right] \quad (26)$$

Rosenthal also offered a 2D solution when a heat source is traveling along a thin plate and has been used to model temperature in laser deposition processes [38-42]. A dimensionless form is offered by et al [40] seen below in Equation 27 with K_0 indicating a second kind, zero order modified Bessel function:

$$\bar{T} = e^{-\bar{X}_0} K_0\left(\sqrt{\bar{X}_0^2 + \bar{Z}_0^2}\right) \quad (27)$$

Where,

$$\bar{T} = \frac{T - T_{base}}{\alpha Q/_{\pi k t}} \qquad \bar{X} = \frac{x}{2k/_{\rho C_p V}} \qquad \bar{Z} = \frac{z}{2k/_{\rho C_p V}} \quad (28)$$

and αQ is the absorbed power, V is the laser velocity, t is thickness of the substrate, x is the axis of the travel path, and z is the axis normal to the substrate. Ignoring the z direction, keeping x constant and equal to a and t equal to 2a, and using the definition of thermal diffusivity, the function can be rewritten as Equation 29.

$$\Delta T = \frac{\omega M_z}{2\pi k a}\, e^{-\frac{Va}{2\alpha}}\, K_0\left(\frac{Va}{2\alpha}\right) \quad (29)$$

The modified Rosenthal thin wall approximation is validated by comparing it to the Bessel function exact form. While the half space (Figure 3.8.a) model captures initial moments prior to transferring heat encountering a boundary, the thin wall (Figure 3.8.b) model represents an extreme case for heat from printing becomes trapped in tall thin builds.

a)

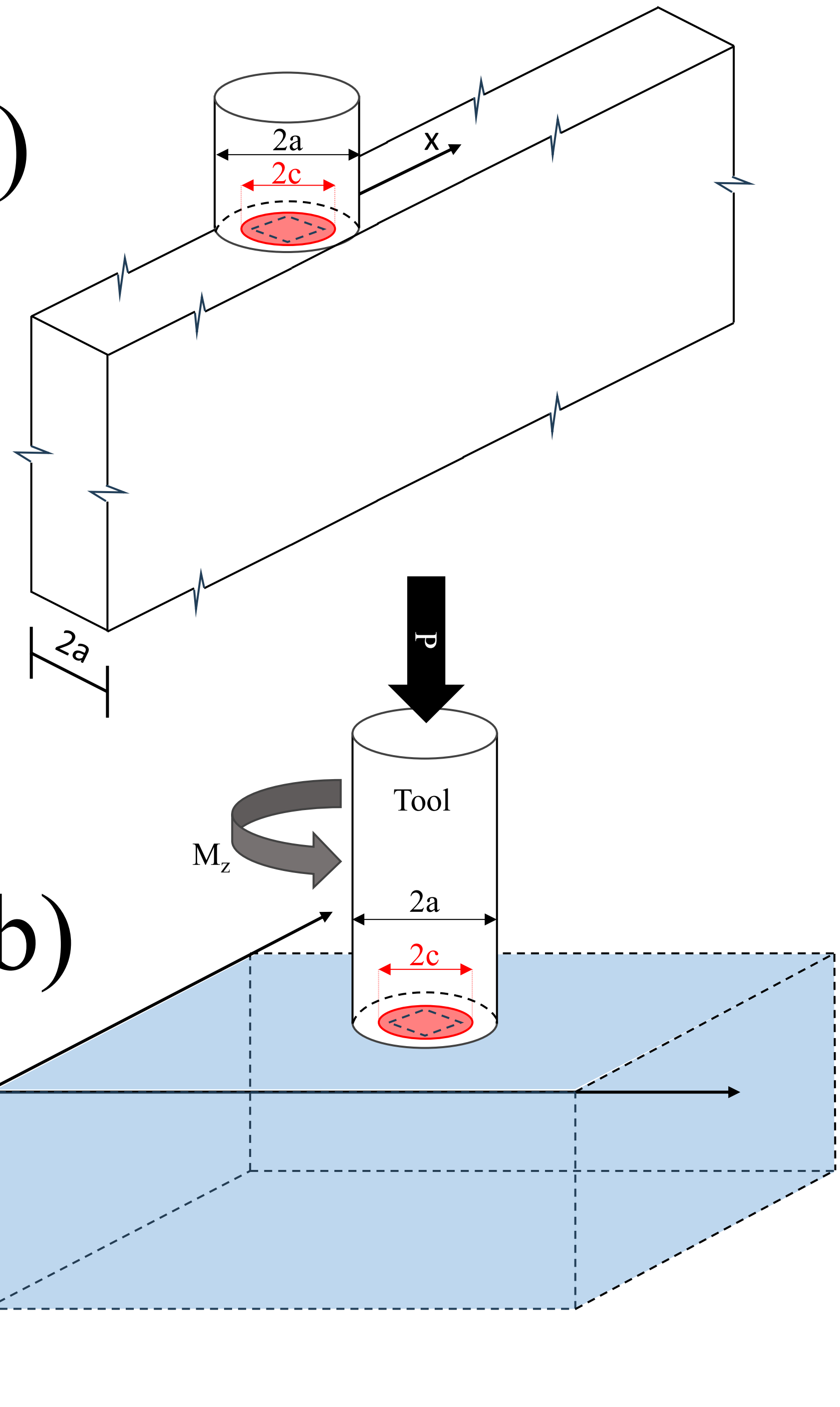

b)

Figure 0.8 AFSD heat source traveling in a a) Thin-Wall and a b) Half-Space

3.4 CEL Simulations

To replicate the deviation from the original model and qualitatively demonstrate its sensitivity to boundary conditions, two simulations were performed using the CEL model developed for FSW using the ABAQUS Explicit Solver equipped with a User Material Subroutine (UMAT) adding the Hyperbolic Creep Sign Law to the solver. Like the experiment, the displacement was predefined, the tool follows the same straight track multiple times, and the system was not given time to return to the ambient temperature between passes. The width of the Eulerian domain decreases from 30 mm to 13 mm for the two jobs. The loads applied to the tool were calculated based on the surface interactions with Eulerian material, aluminum alloy 6061, and material deformation was calculated by tracking volume fraction flux in the non-deformable mesh. The hyperbolic sign law was used to describe material flow using constitutive parameters [43,44] found in Table 3.1. Table 3.2 lists the temperature-dependent material properties [45,56].

Table 0.1 Material parameters for AA6061 Constitutive Model used in the UMAT

A_n (s^{-1})	σ_{ref} (MPa)	n	Q (kJ/mol)
2.41×10^8	22.22	3.55	145

Table 0.2 Temperature dependent material properties for AA6061 used in ABAQUS

Temperature (K)	Specific heat ($Jkg^{-1} K^{-1}$)	Young's modulus (GPa)	Poisson's ratio	Thermal conductivity ($Wm^{-1} K^{-1}$)	Thermal expansion ($10^{-6} K^{-1}$)
298	945	66.94	0.33	162	23.5
373	978	63.21	0.334	177	24.6
422	1000	61.32	0.335	184	25.7
477	1030	56.8	0.336	192	26.6
533	1052	51.15	0.338	201	27.6
589	1080	47.17	0.36	207	28.5
644	1100	43.51	0.4	217	29.6
700	1130	28.77	0.41	229	30.7
755	1276	20.2	0.42	243	-

While heat can conduct and radiate out of the system, the heat transfer through the metal is significantly greater. In modeling FSW, boundary conditions assume surface shearing is constrained along the sides. However, these constraints are removed to create a free surface like the one that is present on the AFSD wall. There is an initial plunge (0.1 seconds at 0.7 mm per second) and dwell (0.2 seconds) to preheat the material before travel (10 seconds at 2mm per second) with the tool spinning at a constant rate of 135 RPM. Once traversing the surface, the tool was lifted and returned to the starting position twice for a total of three passes. The relationship between peak temperature and torque can be seen in Figure 3.9.

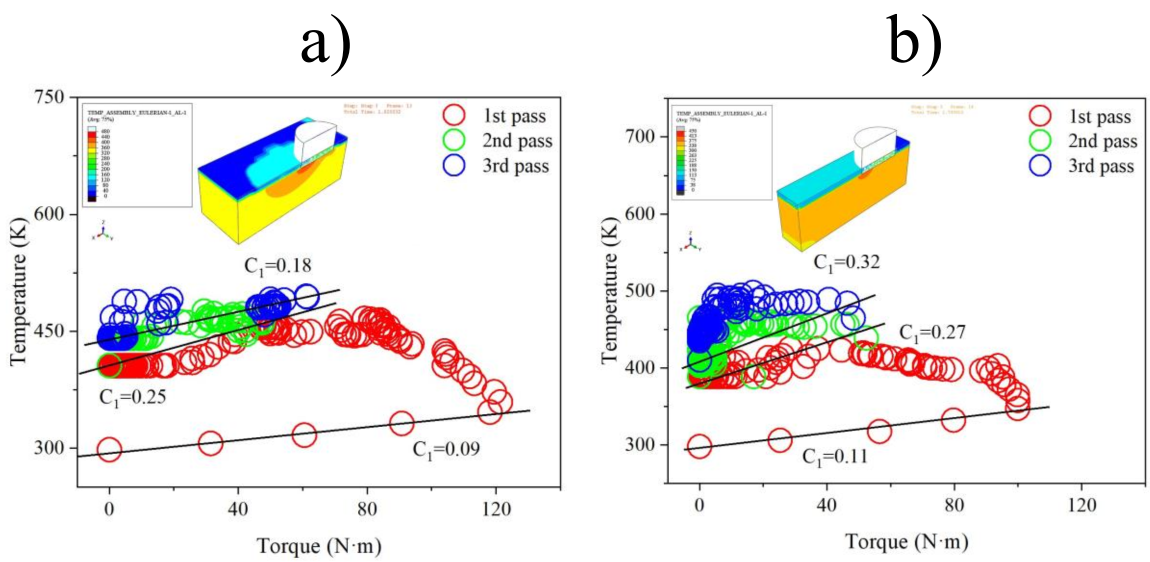

Figure 0.9 CEL of FSW multiple pass simulation a) wide domain b) narrow domain

Initially both datasets follow the same linear path. However, once the Eulerian domain becomes saturated with heat, torque drops as temperature remains elevated. The "7" curve behavior occurs in both simulations, but is more pronounced for the thin wall domain with the turn around occurring at 100 N-m rather than 120 N-m. By the third pass, steady state temperatures are also higher for the thin wall results. Additionally, the slope of the second asymptote is becomes steeper when the thickness of the wall is reduced to the size of the tool.

3.5 Conclusions

The FSW heat generation model was combined with the modified Rosenthal solution. When rewritten into a dimensionless form and plotted with real data from a fixed displacement parametric study (recording torque from the AFSD unit driver and temperature from a thermocouple embedded in the tool), a "7" curve was observed. Plotting in the dimensional form highlighted temperatures of the tool are elevated once travel initiates. Accounting for the preheat from the previous pass as a reference temperature shift resolved issue of the lower part of the "7" curve drifting. However, the turn around that forms the upper portion where torque starts decreasing as the tool approaches end of layer deposition, becoming more pronounced as the height of the wall increases. The Rosenthal equation assumes a semi-infinite half space. The substrate has a limited area and thickness that acts as a conduction barrier. As the heat generated hits these boundaries, the power required to maintain steady state conditions decreases. Therefore, it was hypothesized that the top of the "7" curve deviation behavior would be sensitive to boundary conditions. Two FSW simulations with different widths were conducted. Due to the heavy computation cost of CEL simulations, only three passes were conducted, and a shorter cooldown was used in between each pass to qualitatively demonstrate the effects of boundary conditions. The results confirmed that the drop in torque behavior will vary depending on the setup. However, the model initially predicts the initial heat generation in the experiments and simulations, providing a lower bound and confidence in fundamental understanding of thermomechanics. To predict the upper bound temperature, a thin wall approximation of the modified Rosenthal is proposed. As shown in Figure 3.1.b, the isotherms can be used for a particular temperature range to form a process window. Developing an analytical solution to strain response based on processing parameters will be crucial for predicting bonding behavior of the layers. Together, tensile properties prediction will lead to more processing optimization.

Chapter 4

Characterizing Residual Stress Relaxation of 347AP Weldments using Neutron Diffraction

A version of this chapter was published in the Proceedings of the ASME 2025 Pressure Vessels and Piping Conference (https://doi.org/10.1115/PVP2025-155479). Portions of Chapter One used parts of this publication. Research at Oak Ridge National Laboratory's High Flux Isotope Reactor was sponsored by the U.S. Department of Energy, Office of Basic Energy Sciences.

4.1 Introduction

4.1.1 Abstract

Residual stress formation is an inherent feature of welding processes caused by localized heating, impacting weldment performance. One failure mode associated with welds is stress relief cracking (SRC). In the heat-affected zone (HAZ), elevated temperatures can cause precipitate dissolution. During reheating, whether from post-weld heat treatment (PWHT) or in-service conditions, relaxation occurs simultaneously with the formation of large carbides at grain boundaries. Reprecipitation creates a thin region along the grain perimeter that is deficient in alloying elements. Stress can be resolved by plastically deforming and eventually damaging these weakened regions. Significant research has been focused on understanding precipitate kinetics as the primary cause of failure. Nonetheless, an SRC-susceptible microstructure remains stable in the absence of stress. Therefore, understanding relaxation is necessary to produce mechanism-based lifetime predictions. Although residual stress can be modeled, experimental validation is essential to provide confidence in solutions. Neutron diffraction is generally regarded as the most reliable technique for measuring residual stress. 347H is a common creep-resistant austenitic stainless-steel used in the energy and chemical industries. Driven by the need to improve performance without significantly increasing costs, previous studies have shown that slight adjustments in base metal or filler metal compositions can affect cracking susceptibility. In this study, 347AP austenitic stainless-steel tubes were manually gas tungsten arc welded (GTAW) using both 347AP and 16-8-2 filler rods for comparison, and residual stress measurements were taken before and after PWHT. Measurements were

made at the High Flux Isotope Reactor's High Intensity Diffractometer for Residual Stress Analysis instrument beamline located at Oak Ridge National Laboratory. Although there is confidence neutron diffraction as a reliable residual stress characterization method, challenges still arise when determining reference lattice spacings (d0). Therefore, a plane stress assumption was investigated as a viable alternative to measured d0 fields used to calculate lattice microstrain and ultimately stress fields.

4.1.2 Introduction

The effect of composition on microstructure and stress evolution, regarding SRC behavior of other austenitic stainless steels, has not been thoroughly investigated. 16-8-2 is another creep-resistant austenitic stainless steel that is typically used as a filler metal and has lower alloying element compositions. When used as a filler metal to weld 347H in one study, there was no evidence of SRC during PWHTs [9]. Additionally, 347AP (A proprietary version of 347LN with a higher Nb/C ratio and enhanced stress corrosion cracking properties) demonstrated better SRC resistance when compared to 347H [10]. Based on these previous observations, there is potential for improved performance by altering the material design. The purpose of this study is to explore these candidate materials. However, limited material data for these less common alloys exists, restricting the ability to produce constitutive models. To make accurate lifetime predictions, experiments must be conducted to understand mechanical behavior in response to the welding of these materials. Neutron diffraction is used to understand residual stress formation and relaxation. While computational modeling can simulate residual stress, the penetrating capability of neutrons remains the best method to measure residual stress within a body, providing essential validation for modeling efforts.

4.2 Materials and Methods

4.2.1 Samples: Pipes and Materials

In previous 347H residual stress measurements, Yang used plates that were butt welded. However, 347AP is only commercially available as pipe extrusions and filler material. For this reason, two welds were made using 347AP pipe extrusion. One welded with 347AP filler rod and the other with16-8-2 filler rod.

Table 0.1 Alloying Composition (%wt)

Alloy	Element						
	C	**Si**	**Mn**	**Ni**	**Cr**	**N**	**Nb**
347AP	0.010	0.39	1.50	9.0	17.26	0.07	0.31
347AP Filler	0.03	0.38	1.62	8.29	19.26	0.13	0.41
16-8-2 Filler	0.048	0.38	1.36	7.79	14.97	0.06	-

The tubes were manually GTAW in a butt configuration, resulting in final dimensions that were approximately equivalent. The inner diameter (ID) was ≈75 mm, outer diameter (OD) was ≈90 mm, thickness was 7.6 mm, and length was ≈400 mm with the weld positioned at the center of the pipes.

4.2.2 Neutron Diffraction Setup

Neutron diffraction experiments were conducted at the High Flux Isotope Reactor's (HFIR) High Intensity Diffractometer for Residual Stress Analysis (HIDRA) instrument beamline located at Oak Ridge National Laboratory (ORNL). The high flux of neutrons is ideal for collecting information deep within bulk material. Diffraction is a measurement of lattice spacing (d) of crystal planes, which requires a reference spacing (d_0) to convert to residual strain (ε) then subsequently residual stress (σ).

$$\varepsilon = \frac{d - d_0}{d_0} \tag{30}$$

The (311) family was chosen because the elastic behavior is equivalent to the bulk modulus of austenite. When measuring residual stress in a butt welded plate, a common method for speeding up data collection is to extend the gauge volume in the longitudinal direction (LD) based on a steady state assumption. For piping, the comparable welding direction would be the hoop direction (HD). Due to the curvature of the HD, a larger rectangular volume is impossible, thus a cubic gauge volume (2mm edge length) was utilized throughout these experiments. Other pipe welding directions and their plate relatives include the axial direction (AD) which can be equated to the transverse direction (TD) and the radial direction (RD) which can be equated to the normal direction (ND). The origin of the sample coordinate system is located at the weld centerline and halfway through the thickness of the tube. As shown in Figure 3, a matrix of points was assigned along a RD/AD plane. A higher resolution was implemented in the FZ/HAZ interface region, meanwhile resolution in the base metal (BM) was decreased as the distance from the weld centerline increased.

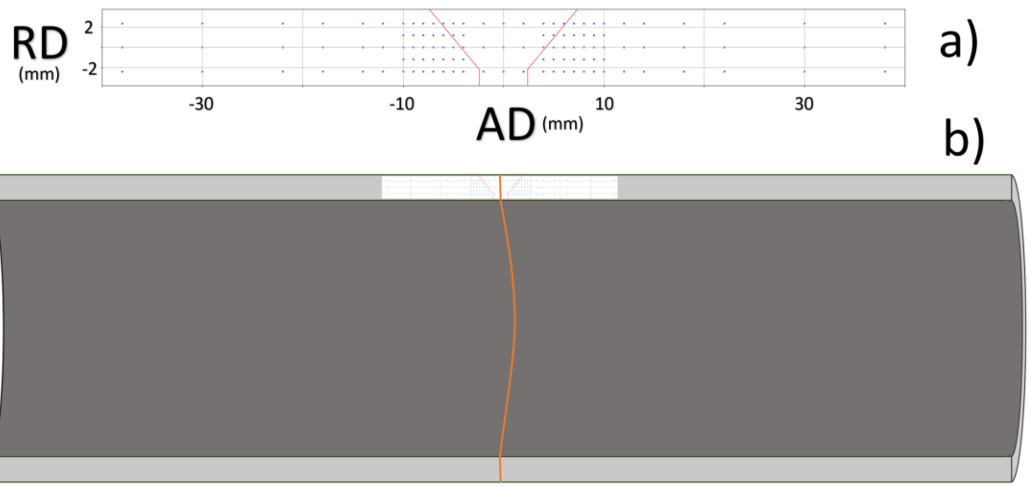

Figure 0.1 Neutron Diffraction Plan: a) Scan matrix with weld groove prior to welding (red) b) Schematic of pipe with scan volume centered along the weld line (Orange)

Moreover, the curvature of the pipe causes material to obstruct the path of the incident beam when taking HD and AD measurements. To provide a clear path for the incident beam and decrease data collection time, slits were machined using an endmill process. However, a side effect of the slits is partial mechanical relief of the residual stress. Because the incident beam for the HD measurement approaches at a 45° angle, a wider slit was required. This larger slit produced a dropout piece that contained a volume that could be used to produce a d_0 reference field. The d_0 reference piece was stress-relieved by cutting out a comb structure using wire electrical discharge machining (EDM). See Figure 4. The need for slits limits the locations that can be readily measured, and therefore rotational symmetry was assumed for the stress field based on a steady-state assumption. Nonetheless, the use of the d_0 comb relies on this assumption as well.

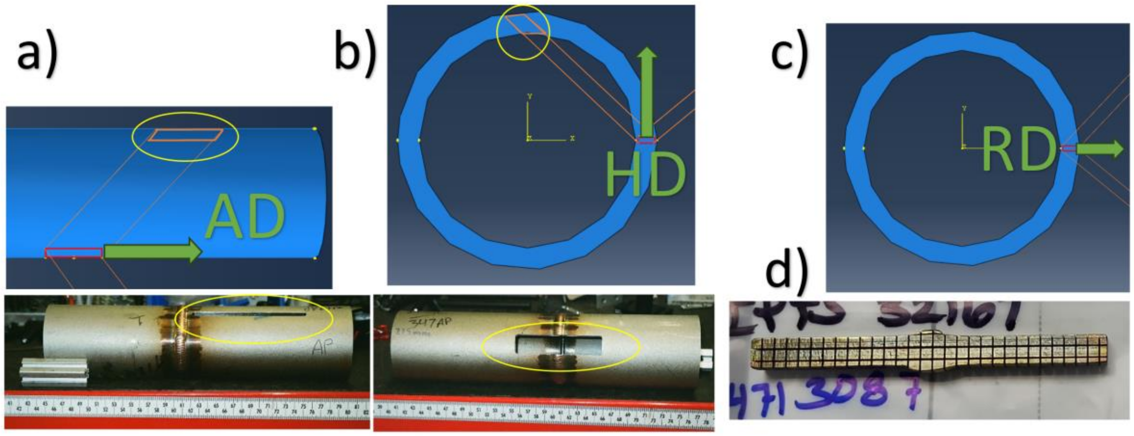

Figure 0.2 Neutron diffraction measurement: (a,b) diagram of Slit, beam path, and scattering vector plus photograph of slits, c) RD diagram, d) d_0 comb sample example photograph (length 80mm)

Two states were analyzed over two instrument cycles: as-welded and PWHT (538℃ for 1 hour + 900℃ for 4 hours). Before each scan set, a standard reference sample was measured for instrument calibration. The tubes (and d_0 combs if needed) were mounted on ad hoc t-slot extrusion structures attached to the instrument stage with x, y, and z motion capabilities. The samples are modeled in this instrument space, and edge scans are performed to precisely align the sample coordinate system to the instrument coordinate system. Tubes were mounted both horizontally to measure the AD and RD (after 90^0 rotation of the stage), and vertically to measure the HD.

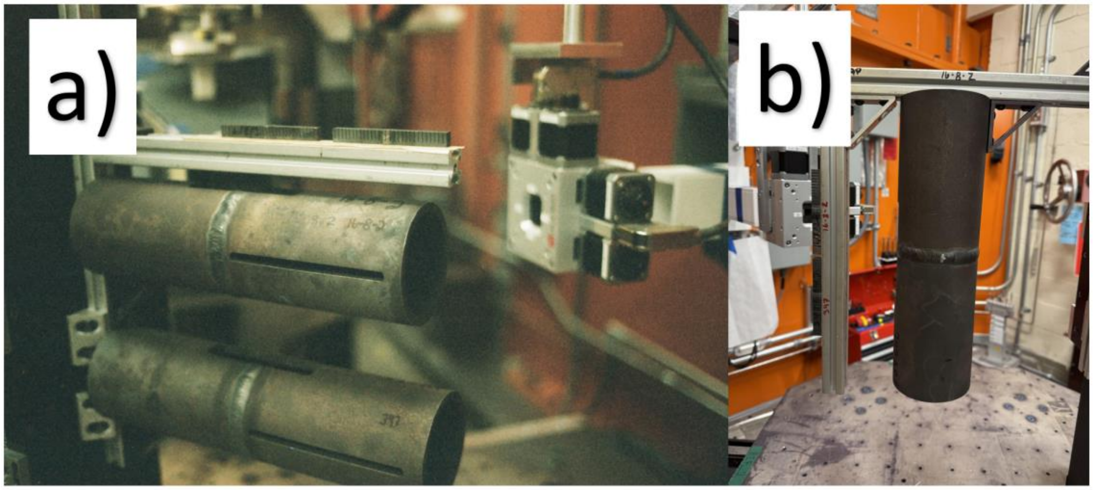

Figure 0.3 Neutron diffraction measurement: Mounting configurations a) Horizontal for AD and RD b) Vertical for HD

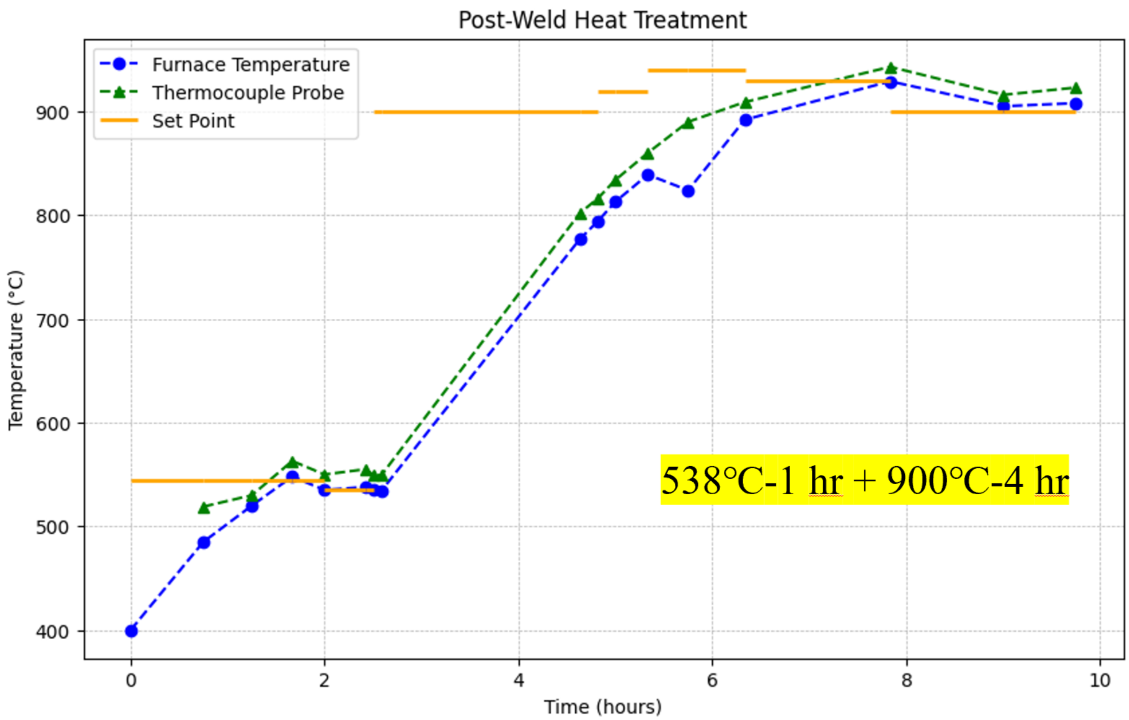

Figure 0.4 PWHT: Furnace setpoint and temperature readout plus thermocouple probe data

After the as-welded measurements were completed, the pipes and combs underwent the PWHT in a box furnace. Roughly 50mm were required to be shaved off the ends of the tubes so that they would fit through the furnace aperture (length of tubes now roughly 300mm). Both the furnace controller and a thermocouple probe were used to monitor the temperature. As shown in Figure 6, the set point was raised slightly higher to prevent the PID controller from slowing down before the second ramp finished, which resulted in some degree of overshoot. Once air cooled, samples were returned to HIDRA, and the scans were repeated the next user cycle.

4.2.3 Data Analysis

The software pyRS v1.2.2 was used to analyze the data, as it has been demonstrated to be effective [47]. A python tool developed for HIDRA, pyRS handles both the diffraction peak fitting and stress analysis. Two methods were used to determine the reference d-spacing fields. One utilizing the stress-relieved comb samples and the other from an assumption that radial stress is zero due to the thin-walled geometry of the tube. In previous work, Yang showed that a plane stress assumption reasonably produced stress maps for 347H welded plates (25.4mm thick) when compared to results using a d_0 field derived from measuring a relieved comb structure d_0 sample.

In addition to understanding the mechanics of the candidate materials, this study aims to investigate whether the radial stress component can be assumed to be negligible, which reduces the time per point by eliminating the need for a comb measurement. The assumption also only relies only on data taken from true locations, removing any uncertainty from assuming radial symmetry of the microstructure. Both d_0 methods rely on Hooke's law, Equation 31, and the assumption that the three tube geometry directions correspond to the three principal stress directions.

$$\sigma_{ii} = \frac{E}{(1+\nu)}[\varepsilon_{ii} + \frac{\nu}{1-2\nu}(\varepsilon_{11} + \varepsilon_{22} + \varepsilon_{33})] \tag{31}$$

Young's modulus and Poison's ratio are assumed to be constant (E = 200 GPa and ν = 0.3). Principal strain components are calculated using Equation 30 and all four data sets (AD, HD, RD, and d_0 comb measurements). However, if a plane stress assumption is made, d_0 values can also be calculated using Equation 35.

$$\sigma_{RD} = \frac{E}{(1+\nu)}\left[\varepsilon_{RD} + \frac{\nu}{1-2\nu}(\varepsilon_{HD} + \varepsilon_{AD} + \varepsilon_{RD})\right] = 0 \tag{32}$$

$$\varepsilon_{RD} = -\frac{\nu}{1-\nu}(\varepsilon_{HD} + \varepsilon_{AD}) \tag{33}$$

$$\frac{d_{RD} - d_0}{d_0} = -\frac{\nu}{1-\nu}\left(\frac{d_{HD} - d_0}{d_0} + \frac{d_{AD} - d_0}{d_0}\right) \tag{34}$$

$$d_0 = \frac{\nu}{1+\nu}(d_{HD} + d_{AD}) + \frac{1-\nu}{1+\nu}d_{RD} \tag{35}$$

4.3 Results and Discussion

4.3.1 As-Welded State

Unfortunately, full scans of the d_0 combs were not performed due to setbacks and limited beam time. To address this, missing data points were estimated by curve fitting rows of d_0 comb values (RD = -2.4, 0, and 2.4), then interpolating these solutions in the higher resolution area and copying RD = 0 solutions in the lower resolution outer regions. The omitted scan points are shown in Figure 4.5. A second d_0 field was generated from the plane stress assumption using Equation 35. Figure 4.6 shows a comparison of these two fields. In all d_0 solutions, relatively small and homogeneous d-spacing values are seen throughout the BM. The d-spacing values increase near the FZ, peaking towards the outer surface of the weld where the weld grove was widest. This trend is more pronounced in the 347AP filler tube. The comb results appear smoother because of the compromised fitting method required to produce a full matrix. Aside from this difference, the solutions to the different approaches were similar. This similarity is reflected in the stress analysis shown in Figures 4.7 and 4.8.

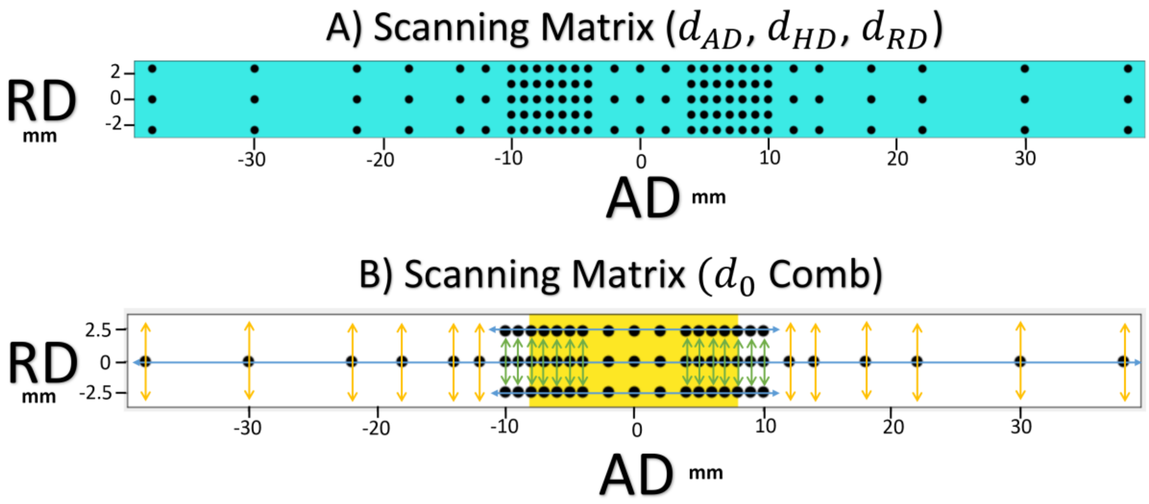

Figure 0.5 a) Complete Scanning matrix compared to b) the compromised Scanning Matrix: Blue arrows indicate the curve fit lines, Green arrows indicated where values were interpolated, and Yellow arrows indicating where points values were extrapolated

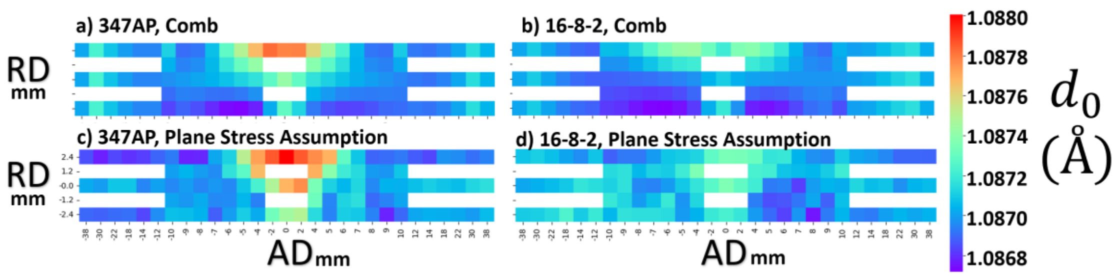

Figure 0.6 The d_0 fields (not to scale) with color bar representing the reference d-spacing (a,b) Comb method, (c,d) Plane Stress Assumption, (a,c) 347AP Filler Tube, (b,d) 16-8-2 Filler Tube

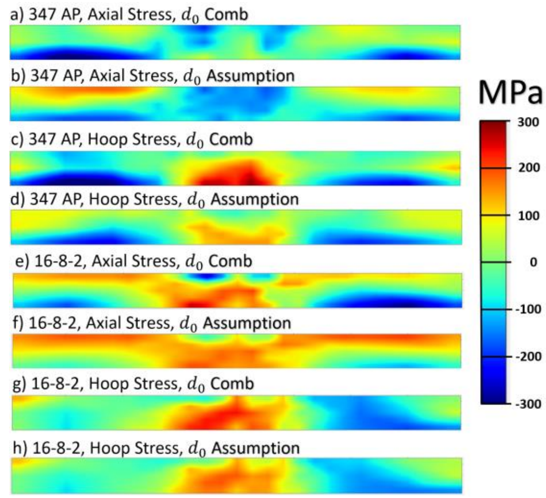

Figure 0.7 Stress Heat Maps warm colors are in tension and cooler colors are in compression (a,b,c,d) 347AP Filler, (e,f,g,h) 16-8-2 Filler, (a,b,e,f) Axial Stress Field, (c,d,g,h) Hoop Stress Field, (a,c,e,g) d_0 Comb, (b,d,f,h) Calculated d_0 (plan-stress assumption)

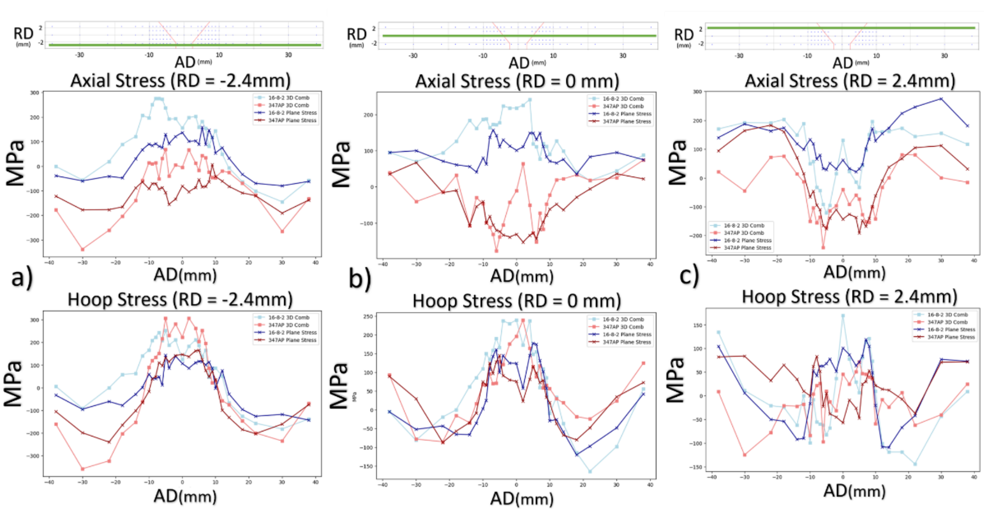

Figure 0.8 Stress Distribution Scatter Plots: 347AP points plotted in red, 16-8-2 points plotted in blue, square points represent stress derived from measured d_0 values, cross marks represent stress derived from plane stress assumption (A) RD = -2.4mm line scan data points (B) RD = 0 mm line scan data points (C) RD = 2.4mm line scan data points

Examining the differences in the d_0 approaches, stress values in the comb analyses tend to be slightly amplified. Additionally in the comb analyses, there are examples in Figure 4.8 (b,c) where sharp deviations from general stress distribution are observed. The hoop stress for all four datasets (both d_0 analyses and filler metals) follows a typical residual stress trend; tension near the weld centerline and the balancing compression towards the outside border of the scan matrix. For the axial stress datasets, shifts are observed near inner and outer edges of the tube, Figure 4.8 (a, c), meanwhile trends at center of the thickness (RD = 0 mm) are flipped when comparing the two tubes. Kou [48] notes that in butt welded plates, LD stresses exhibit the typical compression-tension-compression trend, whereas TD stresses fluctuate to balance stress depending on external constraints during welding, as well as other boundary conditions. The inconsistencies of the axial results can be explained by these reaction stresses.

4.3.2 PHWT State

For the second measurement set, established methods from the as-welded experiment were applied. With most parameters previously programed and no issues occurring, time allowed for two full d_0 comb scans to be completed. As shown in Figure 4.3, comb samples were mounted in both the horizontal and vertical orientations, so AD and HD d_0 measurements could be performed. A comparison of these measured d_0 fields is presented in Figure 4.9. Like the as-welded comb measurements, a roughly homogenous field of smaller d-spacing values is observed outside the FZ. However, this overall trend is shifted up for the HD scan. This difference could have resulted from the shape of the comb structure. The AD is perpendicular to the teeth of the comb structure, whereas the HD is parallel. This means the length from free surface to free surface is 2mm in the AD, while 10mm in the HD. However, the combs also underwent the PWHT, which should have largely relieved residual stress in addition to machining. Similarly, the tubes themselves were expected to be nearly stress free from the PWHT. However, this is not reflected in either of the d_0 comb stress analyses. The stress state derived from the two comb measurements are shown in Figure 4.10. Reviewing the results, there is a high dependence on which directional measurement was used. Comparing hoop stress versus axial stress for a given sample, there is little variation. Furthermore, there is no discernible trend with seemingly random “hot” and “cool” spots.

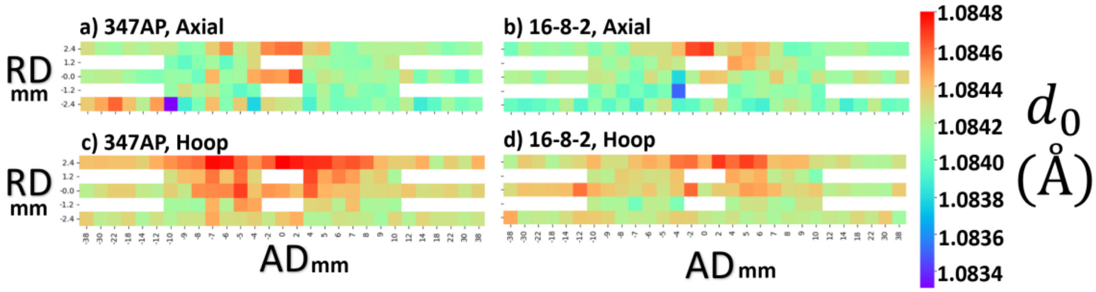

Figure 0.9 The d_0 fields (not to scale) (a,b) AD Comb measurement, (c,d) HD Comb measurement, (a,c) 347AP Filler Tube, (b,d) 16-8-2 Filler Tube

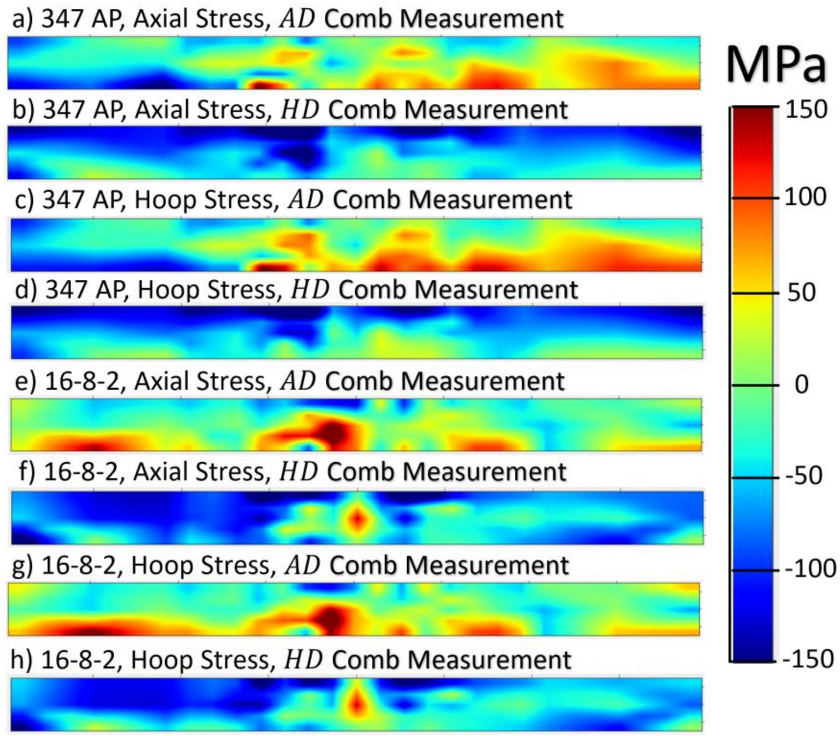

Figure 0.10 Comparing the two directional measurements (AD and HD) of the d_0 Combs using Stress Heat Maps (warm colors are in tension and cooler colors are in compression) (a,b,c,d) 347AP Filler, (e,f,g,h) 16-8-2 Filler, (a,b,e,f) Axial Stress Field, (c,d,g,h) Hoop Stress Field, (a,c,e,g) d_0 Comb, (b,d,f,h) Calculated d_0 (plan-stress assumption)

The average stress of the AD d_0 comb stress analyses are closer to the expected relieved state. Therefore, these results will be used when comparing to the plane stress approach stress fields shown in Figures 4.11 and 4.12. For the d_0 comb stress fields, the data is sporadic and exhibits larger uncertainty. However, for the plane stress assumption results, clear trends emerged. While the 16-8-2 filler tube appears to be mostly relieved, the 347AP filler tube shows more noticeable retention of residual stress. In the FZ, compression is observed, particularly near the outer surface of the solidified weld pool, while tension is observed in the HAZ, especially near the inner diameter of the tube. These trends are present in both the axial and hoop stress analyses but are more pronounced in the hoop results.

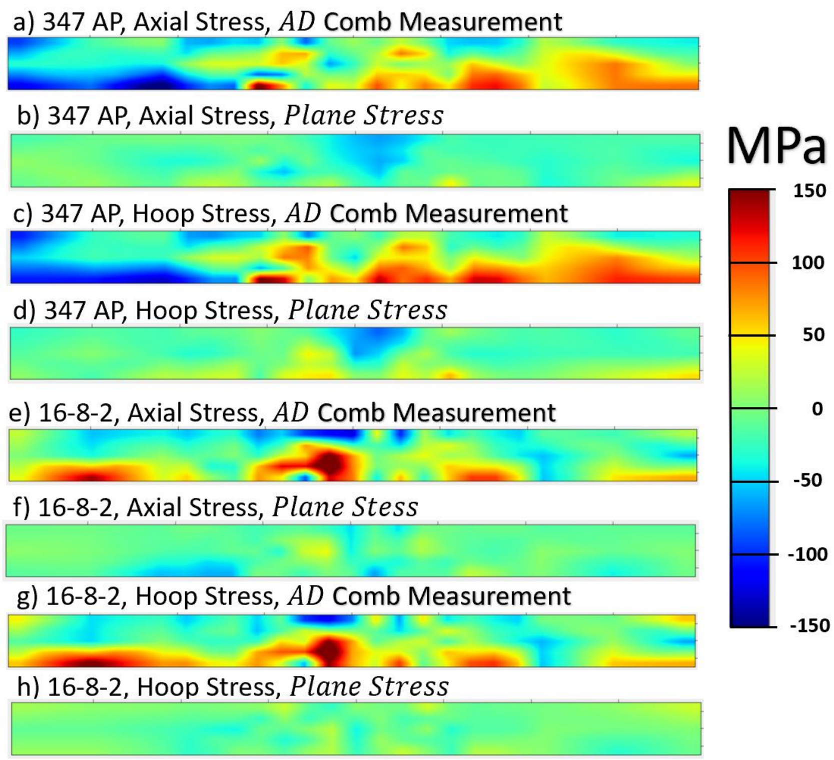

Figure 0.11 Comparing the two directional measurements (AD and HD) of the D_0 Combs using Stress Heat Maps (warm colors are in tension and cooler colors are in compression) (a,b,c,d) 347AP Filler, (e,f,g,h) 16-8-2 Filler, (a,b,e,f) Axial Stress Field, (c,d,g,h) Hoop Stress Field, (a,c,e,g) d_0 Comb, (b,d,f,h) Calculated d_0 (plan-stress assumption)

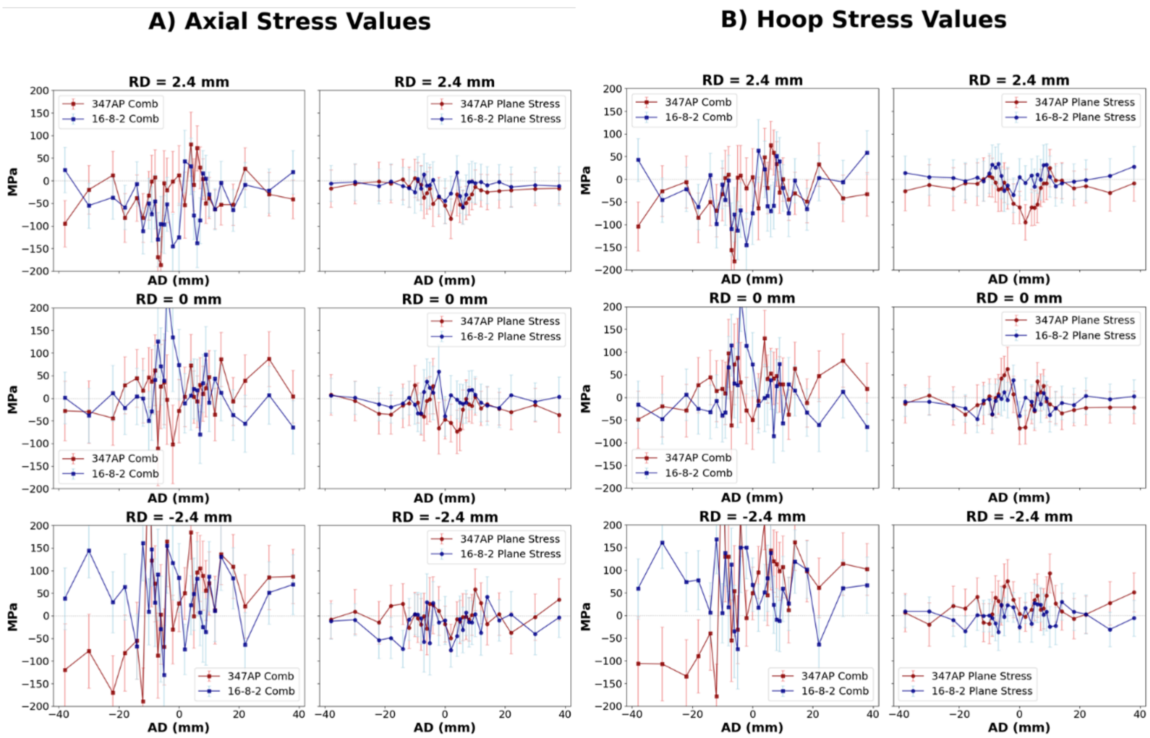

Figure 0.12 Stress Distribution Scatter Plots: 347AP points plotted in red, 16-8-2 points plotted in blue, square points represent an ad measured d_0 analysis, circular marks represent a calculated d_0 analysis a) AD b) HD

4.3.3 Discussion

Determining the accuracy of the d_0 methodologies was initially challenging with only as-welded results. However, the PHWT conditions provided an expectation of a relaxed state. Inferred from Equation 29, small changes in d_0 would significantly impact strain estimations, and consequently stress analyses. In addition to the benefits mentioned in the introduction for using the plane stress assumption (i.e. less time per point and only true location information), an underlying advantage could be the use of multiple measurements to formulate d_0. It is hypothesized that the improvement of the PWHT plane stress analyses was due to error fluctuations in peak fits being dampened when results were combined in Equation 34. The curve fitting necessary for a full comb d_0 field in the as-welded state would effectively achieve similar results by smoothing variations, likely contributing to the difficulty when first attempting to contrast the two d_0 approaches.

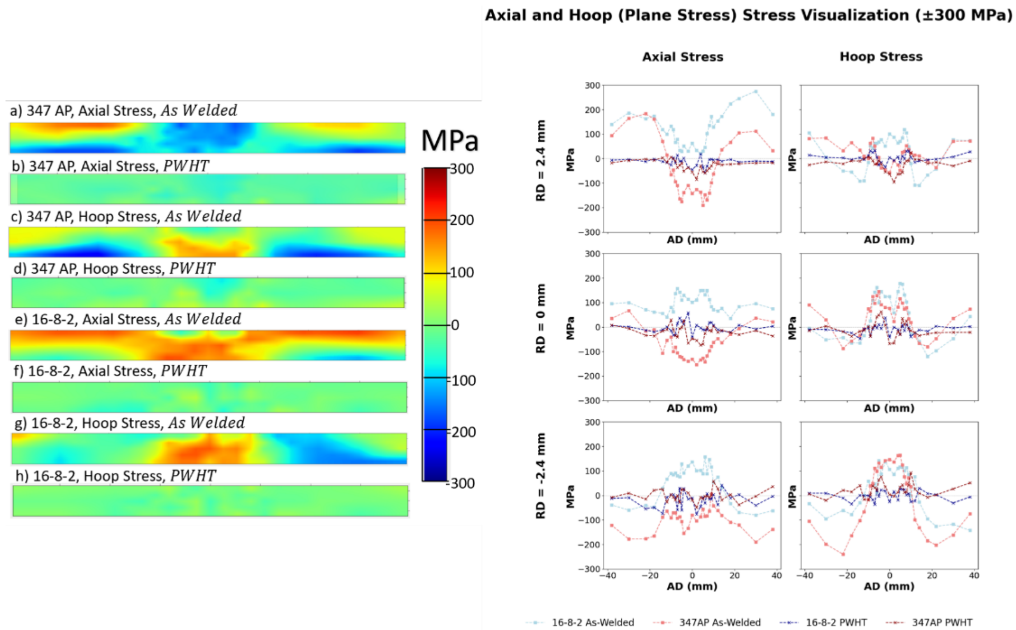

Figure 0.13 All Plane Stress Data: Stress Heat Maps and scatter plots (near OD, Center of thickness, and near ID) with a ±300 MPa scale bar

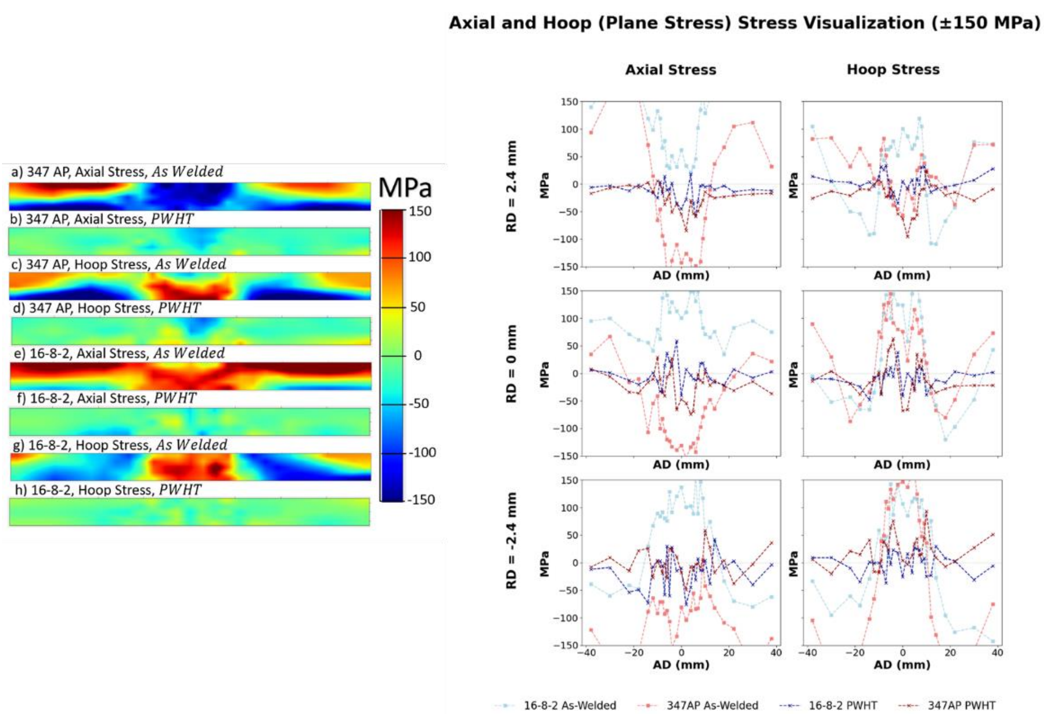

Figure 0.14 All Plane Stress Data: Stress Heat Maps and scatter plots (near OD, Center of thickness, and near ID) with a ±150 MPa scale bar

Only the plane stress assumption is applied for a final comparison of the as-welded versus PWHT conditions, the axial versus hoop stresses, and filler metals, seen in Figures 4.13 and 4.14.

Scales of ±300 MPa and ±150 MPa were used to highlight details for both the as-welded and PWHT results respectively. In the as-welded state, the BM experiences both tension near the OD (100 to 200 MPa) and compression near the ID (-100 to -200 MPa). Residual stress was expected to taper off near ends of the scan matrix, far from the weld centerline. However, the overall size of stress fields was underestimated. After the heat treatment, the BM becomes virtually relieved in all cases.

Excluding the axial stress results of the 347AP filler tube (attributed to reactionary stresses), the as-welded HAZs are almost entirely in tension with highest values occurring at the center of the thickness (100 to 150 MPa). After the PWHT, the HAZ still experienced tension in the 347AP filler tube, particularly the hoop stresses near the ID (50 to 75 MPa). Continuing to ignore the axial stress of the 347AP filler tube, tension in the as-welded FZ is highest near the ID (≈100 MPa) and decreases moving towards the OD (±50 MPa range). After the PWHT, the FZ transitions to compression in the 347AP filler tube, with notable hoop stress at the weld centerline, near OD (≈ -100 MPa).

As mentioned, the 16-8-2 filler tube showed slightly higher residual stress formation compared to the 347AP filler tube, yet the 16-8-12 FZ/HAZ was effectively relieved by the PWHT, while the 347AP FZ/HAZ was not. The difference in relaxation behavior suggests that PWHTs would be more effective in reducing SRC risks in 16-8-2 weldments. 16-8-2 may also exhibit higher SCR resistance in the as-welded state despite demonstrating less creep resistance in these results. When constant load creep-rupture tests (593ºC) were conducted on specimens of 316H stainless steel welded with 16-8-2, they demonstrated creep-rupture ductility across a range of 10-40% [13]. Furthermore, when weld wire arc deposits were tested for their creep-rupture ductility similar results were shown for 16-8-2 but not 347H [14]. Feed material was deposited using GTAW. A variety of austenitic filler materials were examined including 16-8-2 specimens (measured at 650 ºC) and 347H (measured at 550-700 ºC). The elongation at rupture results were in the 10-20% range for 16-8-2, while 347H results were in the 2-6% range, a significant decrease from 347H wrought material performance. Although not much has been published on 347AP, some preliminary work suggests a similar drop in creep ductility when comparing wrought 347AP to welded 347AP.

4.4 Conclusion

Two 347AP tubes were welded using 347AP and 16-8-2 filler metals. Residual stresses in both tubes were measured using neutron diffraction in both the as-welded and PWHT states. While the 16-8-2 tube exhibited higher levels of tensile stress in the HAZ, it also demonstrated faster relaxation behavior. This suggests the creep resistance of 16-8-2 is lower than that of 347AP. However, this may benefit the SRC resistance of 16-8-2 weldments as a PWHT can relieve stress to a higher degree and 16-8-2 welds have shown to exhibit better Monkman-Grant ductility. Under the assumption the behavior of 347AP to 347H weldments are somewhat similar, 347AP/347AP piping would have poorer performance when compared to piping welded with 16-8-2 at intermediate temperatures. However, this may not be the case in higher temperature applications.

Further investigation into the mechanical performance at the various loads, temperatures, and regions of the welded materials is critical to understanding SRC resistance of these materials. To study mechanical properties across a microstructure gradient, fixed-strain thermomechanical tests coupled with digital image correlation (DIC) of weld coupons (347AP/347AP and 347AP/16-8-2) are planned. Additionally, future neutron diffraction experiments are planned to measure stress relaxation at various times during 530ºC thermal exposure to simulate an in-service condition for a 347AP/347AP welded tube (nearly identical to the one in the study). Taking multiple measurements will help with understanding the dynamic relaxation behavior within the tube. However, due to taking multiple snapshots, the scan matrix will need to be thinned from 115 to 87 points and the plane stress assumption will be utilized, increasing efficiency and accuracy. Also, without the need for a d_0 reference comb sample, slits will not be machined. Although this will increase data collection time, the true stress states can be observed using a fully non-destructive approach. Preliminary results demonstrating the stress rebalancing can be found in the appendix.

List of References

[1] Stout RD. *Weldability of steels*. 4th ed. New York: Welding Research Council; 1987.

[2] Cai W, Daehn G, Vivek A, Li J, Khan H, Mishra RS, et al. A state-of-the-art review on solid-state metal joining. *J Manuf Sci Eng*. 2019;141(3). doi:10.1115/1.4041182

[3] Siefert JA, David SA. Weldability and weld performance of candidate austenitic alloys for advanced ultrasupercritical fossil power plants. *Sci Technol Weld Join*. 2014;19:271–94.

[4] David SA, Chen J, Gibson BT, Feng Z. Intelligent weld manufacturing: role of integrated computational welding engineering. In: *Transactions on intelligent welding manufacturing*. Singapore: Springer; 2017. p. 3–30. doi:10.1007/978-981-10-7043-3_1

[5] Thomas WM, Nicholas ED, Needham JC, Murch MG, Temple-Smith P, Dawes CJ. Friction stir butt welding. International patent application PCT/GB92/02203; 1991.

[6] Nandan R, DebRoy T, Bhadeshia H. Recent advances in friction-stir welding – process, weldment structure and properties. *Prog Mater Sci*. 2008;53(6):980–1023. doi:10.1016/j.pmatsci.2008.05.001

[7] Kandasamy K. Solid state joining using additive friction stir processing. United States patent US9511445B2, MELD Manufacturing Corporation; 2016.

[8] Gopan V, Leo Dev Wins K, Surendran A. Innovative potential of additive friction stir deposition among current laser based metal additive manufacturing processes: a review. *CIRP J Manuf Sci Technol*. 2021;32:228–48. doi:10.1016/j.cirpj.2020.12.004

[9] Srivastava M, Rathee S, Maheshwari S, Noor Siddiquee A, Kundra TK. A review on recent progress in solid state friction based metal additive manufacturing: friction stir additive techniques. *Crit Rev Solid State Mater Sci*. 2018;44(5):345–77. doi:10.1080/10408436.2018.1490250

[10] Siefert JA, David SA. Weldability and weld performance of candidate austenitic alloys for advanced ultrasupercritical fossil power plants. *Sci Technol Weld Join*. 2014;19:271–94.

[11] Yang Y, Han D, Gao YF, Zhang W, Bunn JR, Payzant EA, et al. Residual stress modeling and advanced diffraction measurements of 347H steel weldments. In: *Proc ASME Pressure Vessels & Piping Conf*. PVP2022-85608; 2022.

[12] Wang Y, Yang Y, Gao YF, Penso J, Feng Z. A study of stress relaxation cracking mechanism in a 347H steel pipe-shoe weldment after five-year service. In: *Proc ASME Pressure Vessels & Piping Conf*. PVP2023-105755; 2023.

[13] Wang Y, Yang Y, Gao YF, Penso J, Feng Z, Bunn JR, et al. Residual stress in 347H weldments: influence of various thermal treatment on residual stress reduction. In: *Proc ASME Pressure Vessels & Piping Conf*. PVP2024-124579; 2024.

[14] Sarich C, Alexandrov B, Benatar A, Penso J. Test for stress relief cracking susceptibility in creep resistant chromium molybdenum steels. *Sci Technol Weld Join*. 2022;27:265–81.

[15] Pickle T, Augustine C, Yu Z. Mechanical failure risk management for in-service CSP nitrate hot tanks. Golden (CO): National Renewable Energy Laboratory; 2024. Report No.: NREL/TP-5700-87615. Available from: https://www.nrel.gov/docs/fy24osti/87615.pdf

[16] Pickle T, Hong Y, Augustine C, Vidal J, Yu Z. Stress relaxation cracking in 347H stainless steel arc welds: susceptibility evaluation of heat-affected zone. *Metals*. 2024;14:494.

[17] Yang Y, Han D, Zhang W, Gao YF, Penso J, Feng Z. Identifying multiple synergistic factors on the susceptibility to stress relaxation cracking in variously heat-treated weldments. *Mech Mater*. 2024;195:105013.

[18] Wang X, Gao YF, McDonnell M, Feng Z. On the solid-state-bonding mechanism in friction stir welding processes. *Extreme Mech Lett*. 2020;37:100727.

[19] Wang X, Gao YF, Liu X, McDonnell M, Feng Z. Tool-workpiece stick-slip conditions and their effects on torque and heat generation rate in the friction stir welding. *Acta Mater*. 2021;213:116969.

[20] Wang X, Gao YF, McDonnell M, Feng Z. Determination of the friction stir welding window from the solid-state bonding mechanics under severe thermomechanical conditions. *Materialia*. 2022;21:101350.

[21] Gangwar K, Ramulu M. Friction stir welding of titanium alloys: a review. Mater Des. 2018;141:230–55. doi:10.1016/j.matdes.2017.12.033

[22] Raut N, Yakkundi V, Vartak A. A numerical technique to analyze the trend of temperature distribution in the friction stir welding process for titanium Ti-6Al-4V. Mater Today Proc. 2021;41:329–34. doi:10.1016/j.matpr.2020.09.336

[23] Nirmal K, Jagadesh T. Numerical simulations of friction stir welding of dual phase titanium alloy for aerospace applications. Mater Today Proc. 2021;46:4702–8. doi:10.1016/j.matpr.2020.10.300

[24] Ortiz-de-Zarate G, Madariaga A, Garay A, Azpitarte L, Sacristan I, Cuesta M, et al. Experimental and FEM analysis of surface integrity when broaching Ti64. Procedia CIRP. 2018;71:466–71. doi:10.1016/j.procir.2018.05.033

[25] Yang J, Wu J, Zhang Q, Han R, Wang K. The simple hyperbolic-sine equation for superplastic deformation and parameters optimization. J Mater Res Technol. 2020;9(5):10819–29. doi:10.1016/j.jmrt.2020.07.076

[26] Panda B, Garg A, Jian Z, Heidarzadeh A, Gao L. Characterization of the tensile properties of friction stir welded aluminum alloy joints based on axial force, traverse speed, and rotational speed. Front Mech Eng. 2016;11(3):289–98. doi:10.1007/s11465-016-0393-y

[27] Gao Y, Xue Z, Yu Z. Failure mode maps of lap joints under the tensile shear testing condition. *Extreme Mech Lett*. 2020;37:100728. doi:10.1016/j.eml.2020.100728

[28] Rosenthal, D., 1946, “The theory of moving sources of heat and its application on metal treatment”, ASME Trans. 68, pp. 849-866.

[29] Gopan V, Leo Dev Wins K, Surendran A. Innovative potential of additive friction stir deposition among current laser based metal additive manufacturing processes: A Review. CIRP Journal of Manufacturing Science and Technology. 2021 Jan;32:228–48. doi: 10.1016/j.cirpj.2020.12.004

[30] Avery DZ, Cleek CE, Phillips BJ, Rekha MY, Kinser RP, Rao HM, et al. Evaluation of microstructure and mechanical properties of al-Zn-Mg-cu alloy repaired via additive friction stir deposition. Journal of Engineering Materials and Technology. 2022 Feb 10;144(3). doi:10.1115/1.4052816

[31] Phillips BJ, Williamson CJ, Kinser RP, Jordon JB, Doherty KJ, Allison PG. Microstructural and mechanical characterization of additive friction stir-deposition of aluminum alloy 5083 effect of lubrication on Material Anisotropy. Materials. 2021 Nov 8;14(21):6732. doi:10.3390/ma14216732

[32] Nemati S, Butler LG, Ham K, Knapp GL, Zeng C, Emanet S, et al. Neutron imaging of al6061 prepared by solid-state friction stir additive manufacturing. Metals. 2023 Jan 17;13(2):188. doi:10.3390/met13020188

[33] Hoarston JB, Strain J, Artzer A, Zettwoch JN, Brewer LN, Jordon JB, et al. Understanding the influence of heat input and deposition pitch on achieving isotropic tensile behavior in large-scale AM OF AA7075 additive friction stir depositions. Additive Manufacturing. 2025 Jul;109:104907. doi:10.1016/j.addma.2025.104907

[34] Garcia D, Hartley WD, Rauch HA, Griffiths RJ, Wang R, Kong ZJ, et al. In situ investigation into temperature evolution and heat generation during additive friction stir deposition: A comparative study of cu and Al-Mg-Si. Additive Manufacturing. 2020 Aug;34:101386. doi:10.1016/j.addma.2020.101386

[35] Griffiths RJ, Garcia D, Song J, Vasudevan VK, Steiner MA, Cai W, et al. Solid-state additive manufacturing of aluminum and copper using additive friction stir deposition: Process-microstructure linkages. Materialia. 2021 Mar;15:100967.

[36] Shi T, Wu J, Ma M, Charles E, Schmitz T. AFSD-nets: A physics-informed machine learning model for predicting the temperature evolution during additive friction stir deposition. SSRN Electronic Journal. 2023; doi:10.2139/ssrn.4627557

[37] Carslaw HS, Jaeger JC. Conduction of heat in solids. Oxford: Oxford University Press; 1959.

[38] Dykhuizen, R.C. and Dobranich, D., "Cooling Rates in the LENS Process," Sandia National Laboratories Internal Report, 1998.

[39] Dykhuizen, R.C. and Dobranich, D., "Analytical Thermal Models for the LENS Process," Sandia National Laboratories Internal Report, 1998.

[40] Vasinonta A, Beuth J, Griffith M. Process maps for laser deposition of thin-walled structures. 1999.

[41] Thompson JR. Relating Microstructure to Process Variables in Beam-Based Additive Manufacturing of Inconel 718. 2014.

[42] Kleindienst J, Bagshaw N, Iten J, Klemm-Toole J. Modeling solidification microstructure in an inoculated aluminum 6061 alloy processed with gas metal arc directed energy deposition. JOM. 2025 Mar;77(3):1423-37. doi:10.1007/s11837-024-07066-4

[43] Sheppard T, Jackson A. Constitutive equations for use in prediction of flow stress during extrusion of aluminium alloys. Materials science and Technology. 1997 Mar 1;13(3):203-9. doi:10.1179/mst.1997.13.3.203

[44] Crawford R, Cook GE, Strauss AM, Hartman DA, Stremler MA. Experimental defect analysis and force prediction simulation of high weld pitch friction stir welding. Science and Technology of Welding and Joining. 2006 Nov;11(6):657-65. doi:10.1179/174329306X147742

[45] Al-Badour F, Merah N, Shuaib A, Bazoune A. Coupled Eulerian Lagrangian finite element modeling of friction stir welding processes. Journal of Materials Processing Technology. 2013 Aug 1;213(8):1433-9. doi:10.1016/j.jmatprotec.2013.02.014

[46] Chao YJ, Liu S, Chien CH. Friction stir welding of al 6061-T6 thick plates: Part II-numerical modeling of the thermal and heat transfer phenomena. Journal of the Chinese Institute of Engineers. 2008 Jul 1;31(5):769-79. doi:10.1080/02533839.2008.9671431

[47] Fancher CM, Bunn JR, Bilheux J, Zhou W, Whitfield RE, Borreguero J, et al. pyrs: a user-friendly package for the reduction and analysis of neutron diffraction data measured at the high intensity diffractometer for residual stress analysis. *J Appl Crystallogr*. 2021;54(6):1886-93.

[48] Kou S. Analysis of residual stress. In: *Welding metallurgy*. 2nd ed. Hoboken (NJ): John Wiley & Sons; 2003. p. 124–6.

[49] Ward A, Blackburn L. Creep and rupture behavior of weld-deposited type 16-8-2 stainless steel at 593 °C. *J Eng Mater Technol*. 1977;99(2):159–67.

[50] Marshall A, Zhang Z, Farrar J. The useful properties of lean austenitic type 16-8-2 weld metals. Metrode Products Limited; 2005. p. 1–13.

APPENDIX

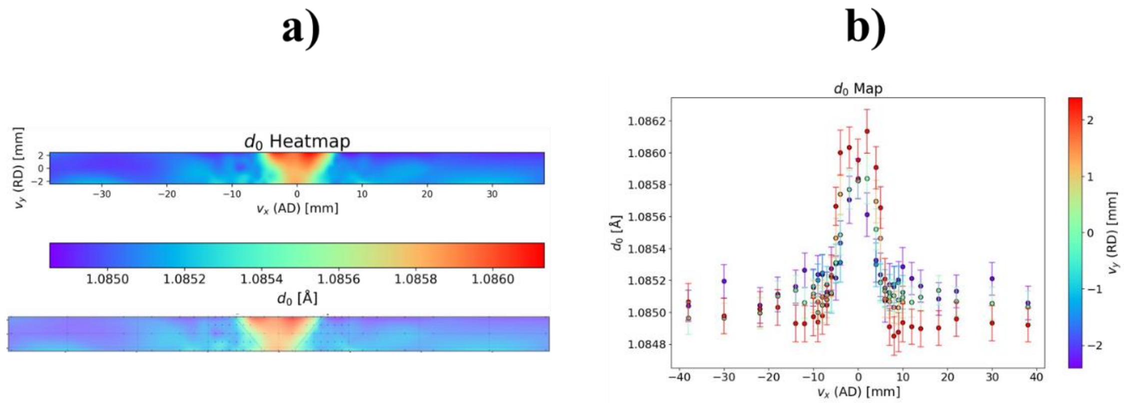

Figure A.1 a) The d_0 heat map from no slit experiment with 347AP/347AP pipe and scan matrix overlay b) The d_0 field revisualized with color bar

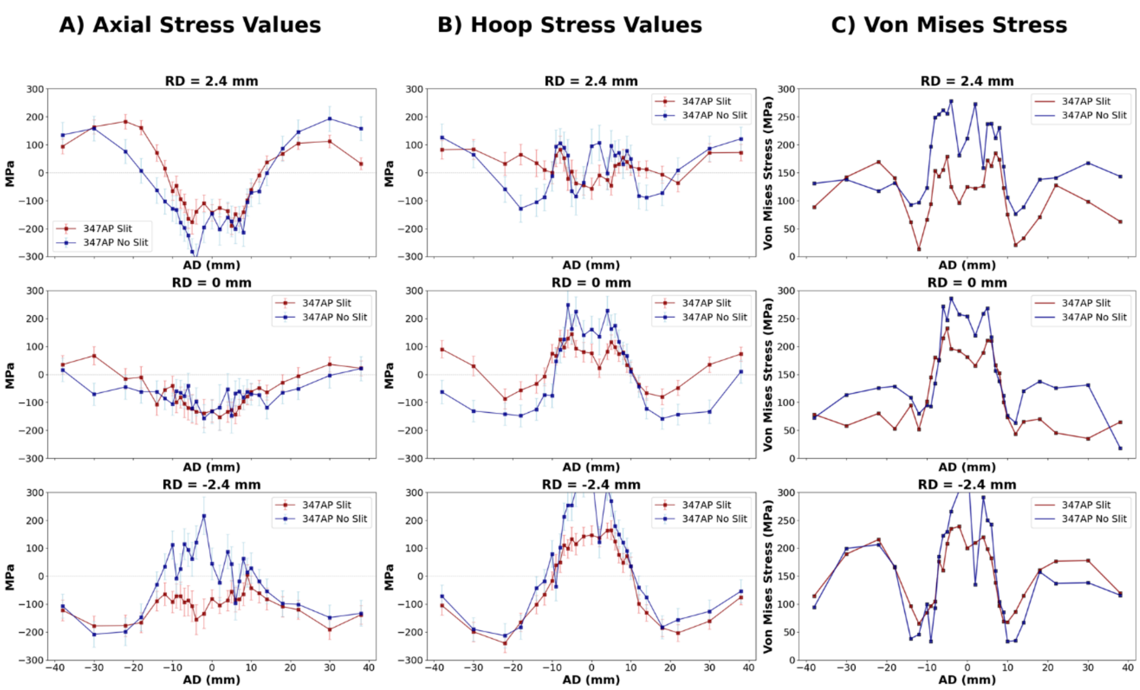

Figure A.2 Line graphs of residual stress values at various depths comparing showing the stress relief from machining slits a) Axial stress b) Hoop stress c) Effective stress

Vita

C. Andrew Kocak was born in 1994 in Charlotte, North Carolina. He obtained a Bachelor of Science degree from the University of Tennessee Knoxville from the department of material science and engineering in 2018. After graduating he worked as an engineer at Aisin Automotive Casting Clinton. He returned to the University of Tennessee Knoxville in the MSE department under the advisement of Prof. Yanfei Gao and Prof. Zhili Feng in 2020 to pursue a Master of Science. After being awarded an MS in 2022, he chose to continue his studies in pursuit of Doctor of Philosophy.